

Peer review status:

This is a non-peer-reviewed preprint submitted to EarthArXiv.

Quantification Error Model for Aerial LiDAR Methane Emission Rate Estimates

Cameron D. Dudiak*, Devin B. Goodwin, Dominic T. Altamura, Christopher P. Donahue, Michael J. Thorpe*

Bridger Photonics, Inc., Bozeman, MT 59718, USA

*Corresponding Authors

Email: Cam.Dudiak@bridgerphotonics.com and Mike.Thorpe@bridgerphotonics.com

KEYWORDS: LiDAR, Remote sensing, Methane, Emissions monitoring, Emission rate quantification error, Gas mapping.

Abstract

Accurate characterization of methane emission rate quantification error (QE) is essential for building measurement-based emissions inventories that benchmark emissions, guide mitigation, and satisfy reporting frameworks such as OGMP 2.0. Previous studies have summarized QE using distributions of errors from controlled release experiments, but with limited consideration of environmental conditions or plume characteristics. We address this gap by developing a continuous QE model as a function of local wind speed and measured signal-to-noise ratio (SNR). Candidate models with diverse functional forms are fitted by maximum likelihood estimation and evaluated using Akaike Information Criterion on a dataset of 2,178 single- and double-blind controlled releases across six test sites scanned with dozens of Bridger Photonics' Gas Mapping LiDAR (GML) 2.0 sensors. Results show that GML QE can be decomposed into two components, bias and uncertainty, where bias is primarily controlled by SNR, and uncertainty is jointly controlled by SNR and wind speed. Bias corrections derived from the model are reinforced by physical principles, providing confidence in their origin and applicability. Applying these corrections to U.S. basin inventories reduces systematic inventory bias by up to 17.5%, enabling more accurate, transparent, and comparable methane emission estimates.

1 Introduction

Reducing atmospheric methane emissions remains one of the most effective near-term strategies for mitigating anthropogenic effects on the climate¹. In the oil and gas sector, methane measurement technologies are increasingly being used to inform leak detection and repair programs through the detection, localization, and quantification of emission sources. They also support measurement-based inventories from operators to basins and nations that are used to benchmark emissions and track progress toward reduction goals. To be useful, these estimates require a well-defined treatment of quantification error that corrects bias where present and

reports uncertainty in a way that is transparent and comparable across time, operators, and regions.

Attempts to quantify methane emissions at scale have historically relied on engineering calculations and sparse on-site measurements². These approaches established the foundation for inventory development, but their dependance on production data and generic emission factors limited their ability to capture the true magnitude and variability of emissions. To bring measurements to scale, the Environmental Defense Fund (EDF) coordinated sixteen large-scale studies from 2012 to 2018 spanning the U.S. oil and gas supply chain using techniques ranging from site-level measurements to regional-scale aircraft surveys and atmospheric sampling networks. This work showed that official inventories underestimated U.S. methane emissions by about 60% on average, with some basins approaching 90%³. At the same time, it highlighted challenges for measurement-based quantification, including long measurement timescales, episodic sampling, and logistical constraints that made accurate, scalable quantification difficult to achieve. These challenges have motivated observation driven methods for developing methane emission inventories.

At the regional scale, satellite observations and atmospheric tower networks coupled with Bayesian inversion models have improved the temporal coverage and produced consistent basin scale emissions estimates^{4,5}. This approach has been valuable because it has produced reasonable estimation of basin-scale emissions and has identified biases in traditional engineering-based inventories. However, satellites remain limited by spatial resolution, detection sensitivity, and quantification uncertainty. Solar-based sensor retrievals are sensitive to cloud cover, solar angle, and surface reflectivity, all of which constrain detection sensitivity and introduce substantial additive uncertainties in emission rate estimation^{6,7}. Similarly, tower networks depend on sparse spatial coverage and local meteorological conditions that complicate the inversion process, making it difficult to attribute measured enhancements to specific sources or in some cases to attribute emissions to specific industry segments (e.g. energy, waste, agriculture).

At the facility scale, some continuous monitoring systems (CMS) provide near-real-time detection and quantification. Recent single-blind evaluations at Colorado State University's (CSU) Methane Emissions Technology Evaluation Center (METEC) have shown improvements across technologies, yet performance remains variable⁸. Quantification continues to be particularly challenging because most CMS solutions infer release rates indirectly from localized concentration data, rather than through direct measurement of entire plumes. This indirect inference introduces substantial model dependence and limits quantification accuracy even under ideal conditions. Additionally, network scalability and false-positive rates limit their use for basin-wide inventory quantification.

Aerial imaging remote sensors provide a practical intermediate solution to address many of these challenges. Aircraft-deployed sensors, including solar shortwave infrared (SWIR)^{9,10}, longwave infrared (LWIR)¹¹, and LiDAR^{12–15}, combine broad survey extent and directly measures plume structure rather than inferring concentrations through modeled dispersion. Each modality

balances sensitivity, coverage, and cost differently, yet all share a central challenge: achieving consistent, well-characterized quantification under variable environmental and operational conditions. Passive infrared (IR) techniques are inherently sensitive to environmental factors. For SWIR systems that rely on reflected sunlight, methane concentration measurements are influenced by solar angles and by variability in surface reflectivity and illumination caused by terrain, vegetation, clouds, and shadows. LWIR measurements depend on thermal contrast and are affected by variable surface emissivity and the temperature difference between the plume and its surroundings. These sensitivities reduce the reliability of plume detection, degrade overall detection sensitivity, and introduce additional sources of quantification error. In contrast, LiDAR methane concentration measurements are much less sensitive to environmental variability because laser spectroscopy provides highly selective detection of methane absorption. Active illumination also allows LiDAR systems to operate independently of sunlight and cloud cover enabling extended temporal monitoring coverage, including nighttime. As a result, LiDAR offers more consistent detection and quantification performance and enables significantly better temporal coverage.

In addition to providing higher accuracy concentration measurements, aerial LiDAR has shown strong potential for producing source-resolved emission estimates with low detection thresholds and well-defined quantification performance. For instance, Bridger Photonics' Gas Mapping LiDAR (GML) achieves a detection sensitivity near 1 kg h⁻¹ at 90% probability of detection for typical scan conditions and is routinely deployed for basin-scale surveys¹⁴. While no single method is completely comprehensive – particularly with respect to spatial-temporal coverage – LiDAR has demonstrated many of the performance requirements essential for producing credible measurement-based methane emissions inventories.

In this work we present a model for characterizing GML quantification error (QE) comprising both systematic bias and random uncertainty. We develop a probabilistic QE framework that extends the methodology of Conrad et al.¹⁶ and explicitly models quantification error as a function of environmental parameters and plume characteristics, such as wind speed, temperature, pressure, concentration, and spatial extent. Using 2,178 controlled-release experiments, we evaluate candidate models and present domain complete and continuous formulations of bias and uncertainty distributions, enabling bias correction and uncertainty quantification across diverse operational conditions.

2 Methods

2.1 Functional Notation

Table 1 summarizes the symbols and definitions used throughout the manuscript for quick reference. Acronyms are defined at first mention and used consistently thereafter. A glossary of terms for utilized acronyms not included in Table 1 are provided in Supporting Information S1, Table S1.

Table 1. Symbols and definitions used throughout the manuscript.

	Definition	Symbol
--	------------	--------

ζ	Average Signal to Noise Ratio (Base-10 Logarithm)
BCF	Bias Correction Factor
ξ	Complete Model Coefficients
ξ^*	Complete Optimized Model Coefficients
CDF	Cumulative Distribution Function
Q	Emission Rate (Actual)
Q Q Q	Emission Rate (Bias-Corrected)
$ ilde{Q}$	Emission Rate (Estimated)
EPE	Estimation Percentage Error
τ	Integrated Plume Concentration (Base-10 Logarithm)
invCDF	Inverse Cumulative Distribution Function
\dot{P}_1	Predictor Function 1
\dot{P}_2	Predictor Function 2
α	Predictor 1 Coefficients
β	Predictor 2 Coefficients
PDF	Probability Density Function
RER	Relative Error Ratio (Actual ER / Estimated ER)
R'	Relative Error Ratio (Base-e Logarithm)
U	Wind Speed

2.2 Data Acquisition

The dataset used in this work consists of 2,178 isolated, non-occluded controlled methane release flyover tests collected from September 2022 to March 2025 across six test sites: Bozeman, Montana (MT), Livingston, MT, Clyde Park, MT, Columbus, MT, Hysham, MT, and Wonowon, British Columbia (BC). These campaigns included both single- and double-blind tests spanning diverse environmental conditions, experimental configurations, and gas flow rates. Data was acquired using several dozen Bridger Photonics' GML 2.0 aerial sensors deployed on Cessna 172 aircraft operating at flight altitudes between 150 and 275 m AGL.

Emission rates were measured with calibrated flow controllers, and wind data was measured using on-site anemometers positioned near the release location at a height of 1.5 - 3 m AGL; Details regarding which anemometers and flow controllers are used can be found in Thorpe et al.¹⁴. Each instrument was paired with a 1-second resolution data logger capturing time-series flow rates and wind speeds. Release heights were chosen to represent mid- and upstream sector source heights (0–3 m AGL). Metered release experiments that were representative of the downstream (distribution) sector were omitted due to extraneous variables and limited coverage across the experimental domain.

Controlled release experiments were conducted following the methodologies described in Thorpe et al. 14 to promote adequate plume development and ensure analyzed plumes correspond to a single emission source. An overview of experimental campaign parameters is shown in Table 2. Metered release flow rates ranged from 0.074 to $64.28 \, \mathrm{kg} \, \mathrm{h}^{-1}$ and were comprised of isolated methane plumes, defined as a single methane source location whose plume does not spatially overlap with any other sources. To preserve a precise definition for

single-plume quantification, flyover passes corresponding to plumes with multiple emission sources or insufficient development time were excluded.

Table 2. Details of experimental campaign parameters conducted for this work. Testing organizations included Bridger Photonics, Inc. (BP) and Carleton University (CU).

Testing Org	Location	Aircraft Type	Test Type	Test Dates	Emission events #	Release height (m)	Flight altitude (m)	Flight Speed (mph)
ВР	Bozeman, MT	Cessna 172	Single-blind	09/07/2022- 09/20/2023	347	1-2	150-220	90-130
ВР	Clyde Park, MT	Cessna 172	Single-blind	09/18/2023- 05/28/2025	848	1.6-2	150-220	85-145
ВР	Livingston, MT	Cessna 172	Single-blind	08/16/2023- 02/27/2025	70	2	150-230	80-135
ВР	Columbus, MT	Cessna 172	Single-blind	02/12/2024- 02/27/2025	484	2	210-260	85-150
ВР	Hysham, MT	Cessna 172	Single-blind	03/07/2025- 03/08/2025	147	2	150-230	80-140
CU	Wonowon, BC	Cessna 172	Single- & double-blind	09/11/2024- 09/14/2024	282	1.15-1.19	205-279	90-120

2.3 Data Processing

The data collected was processed using Bridger's standard processing routines, described in Kreitinger and Thorpe¹⁷. First, LiDAR data enters an automated detection algorithm whereby contiguous spatial and temporal regions of elevated concentration are identified. Detections are then analyzed using Bridger's standard guidelines to determine the emission source location, plume height, and flow rate. A more detailed description of this procedure can be found in Thorpe et al.¹⁴. Although some detected plumes correspond to multiple closely located sources, most of the nearly 1 million source attributed plumes identified by GML to date originate from a single source – this study restricts analysis to only the latter case.

2.4 Selecting Model Physical Parameters.

The first step in developing a QE model was to analyze the controlled-release dataset to identify potential environmental, instrumental, and retrieval parameters that systematically influence emission rate quantification error. Building on prior understanding of plume detection and retrieval physics, we investigated a range of environmental and plume parameters to identify those most strongly associated with quantification bias and uncertainty. Specifically, we examined signal-to-noise ratio of the LiDAR methane concentration measurements averaged across each detection (average SNR), wind speed at the detection location (WS; m s⁻¹), estimated emission rate of the detected source (ER; kg h⁻¹), and integrated plume concentration (IPC; ppm·m²). We also evaluated ancillary parameters such as ambient temperature and pressure to test for potential influence on retrieval performance.

For each parameter, bias and standard deviation of quantification results were plotted to assess systematic trends. Clear dependencies were observed for average SNR, wind speed, emission rate, and integrated plume concentration, while temperature and pressure exhibited

no discernible trends in either bias or uncertainty (see Supplementary Information S3.4). Based on these results, we selected the parameters showing the most consistent relationships for inclusion in subsequent model development, using them to inform the evolution of location and scale parameters of the model link function (or shape, where applicable). This approach ensures that the resulting models are both physically motivated and empirically grounded in observed data behavior.

To explore how QE varied with each parameter, we binned the data into discrete, non-disjoint intervals of the physical variables and examined systematic trends in both bias and uncertainty along the parameter space. For each flyover pass, we computed the relative error ratio (RER), defined as the ratio of the actual emission rate to the estimated emission rate. Within each bin, bias was defined as the mean RER and uncertainty as its standard deviation. These quantities were used to evaluate how quantification performance varied with changes in each physical variable. Parameters were favored when they exhibited smooth, monotonic, and physically interpretable trends, indicating that they capture variation in error in a way consistent with known measurement physics and therefore provide a meaningful foundation for predictive modeling.

Because RER is bound below by zero but unbounded above ($0 < \text{RER} < \infty$), its distribution is inherently asymmetric, with a longer tail toward underestimation (i.e. values of RER greater than one). To normalize this skew, we transformed RER using $R' = \ln$ (RER), which produces a symmetric distribution where underestimation and overestimation are represented equally in magnitude¹⁸. Refer to SI Section S4 for details regarding this transformation. The transformed RER distribution facilitates the use of standard link functions with well-behaved statistical properties. After transformation, candidate link functions were limited to the normal and logistic distributions, each defined by a location parameter corresponding the distribution mean (bias) and a scale parameter corresponding the distribution spread (uncertainty).

The link function parameters were expressed as predictor functions of the physical inputs, allowing the mean and spread of the statistical distribution to vary systematically with environmental and plume characteristics. Physical parameter inputs into the candidate predictor functions considered in this work are defined as:

$$\zeta \coloneqq \log_{10}(\text{average SNR}), U \coloneqq \text{WS}, \tau \coloneqq \log_{10}(\text{IPC}), \text{ and } \tilde{Q} \coloneqq \log_{10}(\text{ER}).$$

For detailed definitions of the predictor and link functions considered in this work, refer to SI Section S6, Tables S2, S3 & S4. Candidate models were fitted to the controlled-release dataset using a two-step procedure. First, we partitioned the observations over the physical parameter space and used ordinary least squares regression to derive initial coefficient estimates for the predictor functions. Second, these estimates were refined using maximum likelihood estimation (MLE) under the specified distribution to obtain optimized coefficients. The complete candidate QE models were then fit by applying the Nelder–Mead Simplex Algorithm (NMSA)¹⁹ to minimize the weighted negative log-likelihood function (NLLF).

Model performance was quantified using the corrected Akaike Information Criterion (AICc)²⁰, which penalizes over-parameterization and enables comparison across models of differing complexity and construction. For each model, AICc was computed as a function of the minimized, unweighted NLLF, the number of optimized coefficients, and sample size. Models were then ranked by relative likelihood of minimizing information loss (RLMIL), with the best-supported model receiving a RLMIL score of 1. A detailed description of this procedure is provided in SI Section S5.

3 Results

Results for bias are presented first, followed by uncertainty, and finally an integrated evaluation of aggregate model performance. For clarity, we define bias as the mean value associated with the defined R' distribution and uncertainty as the standard deviation associated with the defined R' distribution. Bias of the R' distribution will be reported in Estimation Percentage Error (EPE): EPE = $100 \times (\exp(R')^{-1} - 1)$. EPE provides an interpretable representation of estimation error with positive values corresponding to the percentage a measurement is overestimated, and negative values corresponding to the percentage a measurement is underestimated.

3.1 Bias

As shown in Figure 1, trends in the evolution of bias are observed with all physical parameters to various degrees of quality. Relationships involving wind speed (U), integrated plume concentration (τ) , and estimated emission rate (\tilde{Q}) are either weak, in the case of wind speed, or complex, in the case of integrated plume concentration and estimated emission rate. To promote simplicity while maintaining model completeness, predictor functions were constructed to be low order (required to have less than 4 parameters), monotonic, and continuous. Among all parameters, the average signal-to-noise ratio (average SNR, modeled as ζ) emerged as the strongest and most consistent explanatory variable for bias. Figure 1 a) demonstrates that bias decreases steadily and monotonically with increasing ζ , approaching zero bias for high SNR – indicating that detections with strong SNR exhibit negligible systematic bias in measurement.

Physically, ζ represents the degree to which the measured signal exceeds the sensor's noise floor or detection threshold relative to the local atmospheric background concentration during data acquisition. The placement of this threshold determines whether emission rates are systematically under- or overestimated. When signal strength is low relative to the noise floor, the fractional error in estimated emission rate increases. The controlled release data also reveals a systematic bias for detections with low SNR exhibiting overestimation (positive bias) in emission rates, whereas those with SNR display negligible bias, providing accurate measurements of emission rate. Per the definition of RER, bias values less than 1 indicate overestimation (positive bias), while values greater than 1 indicate underestimation (negative bias). Because bias is modeled as $R' = \ln(RER)$, negative values correspond to overestimation, and positive values correspond to underestimation.

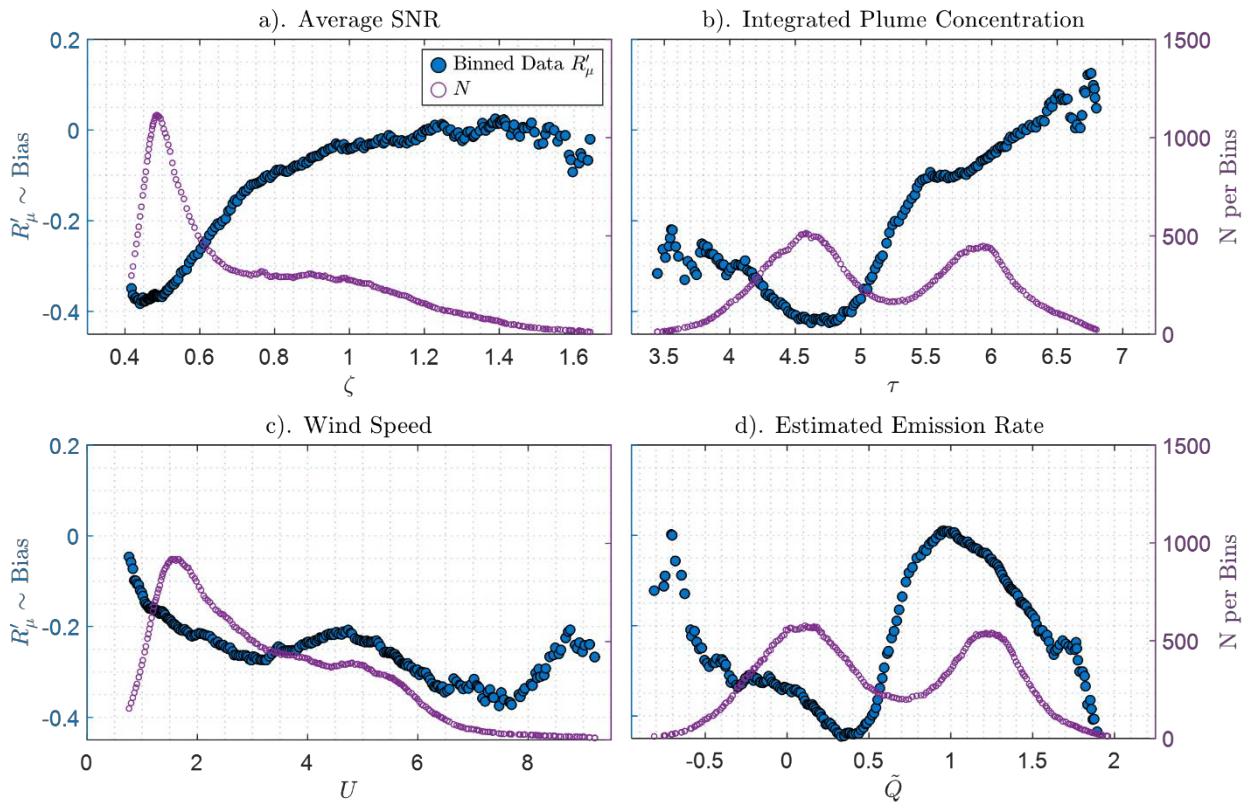


Figure 1. The evolution of bias, measured as the mean, across a): ζ (average SNR); b): τ (IPC – Integrated Plume Concentration); c): U (WS – Wind Speed); & d): \tilde{Q} (ER – Estimated Emission Rate). N is the number of data points per bin.

The best performing predictor functions evaluated in this study are summarized in SI Section S6, Table S2. Predictors for the location parameter are denoted 'A#', and predictors for the scale parameter are denoted 'B#'. The fitted logistic distribution function with predictor function A1, shown in Figure 2, exhibited the best overall performance. It captures the steep decline in bias at moderate ζ values and the asymptotic behavior at the extremes of the domain. The logistic form constrains extrapolation beyond the range of adequate training data density and aligns with the notion that stronger signal-to-noise reduces systematic error.

In the low average SNR regime ($10^{\zeta} \leq 3$), EPE averaged approximately +44% ($R'_{\mu} = -0.365$), indicating substantial overestimation. The EPE decreased to approximately +27% ($R'_{\mu} = -0.239$) in the moderate-range ($3 < 10^{\zeta} \leq 8$) and approached 0% ($R'_{\mu} = 0$) in the high average SNR regime ($10^{\zeta} > 8$). We partitioned the controlled release data by wind speed for the aforementioned ζ regimes and found bias to have no dependence on wind speed.

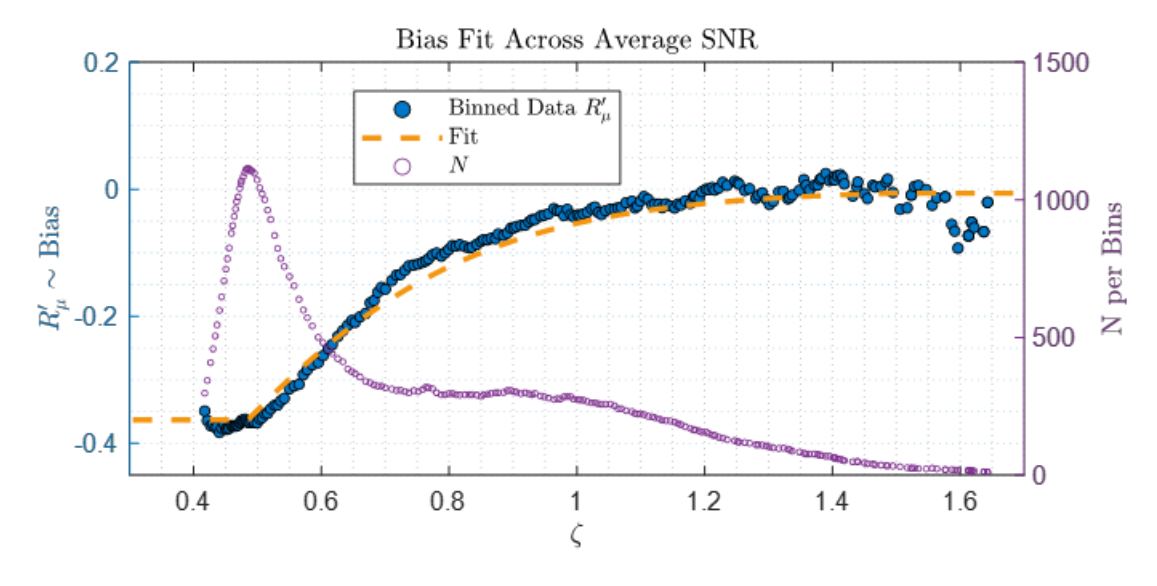


Figure 2. Bias vs ζ , with the complete model fitted bias predictor A1.

3.2 Uncertainty

We analyzed relationships between candidate physical predictors and quantification uncertainty by examining how the standard deviation of binned distributions varied with each parameter. Among these, wind speed (WS; U) exhibited the clearest and most monotonic trend with quantification uncertainty (Figure 3c). Average signal-to-noise ratio (average SNR; ζ), integrated plume concentration (IPC; τ), and estimated emission rate (estimated ER; \tilde{Q}) each showed partial or irregular trends, but none as distinct or consistent as wind speed (Figure 3a, c, & d).

To further explore joint dependencies, we partitioned the data by regimes of average SNR, IPC, and estimated ER and plotted these subsets as functions of WS. This revealed a more systematic, monotonic dependence of uncertainty on average SNR (Figures Figure 4–Figure 5). Applying the fitting procedure described in the previous section to all combinations of WS with average SNR, IPC, and estimated ER confirmed that average SNR provided the most robust and interpretable model performance. These results highlight the dominant role of WS in driving uncertainty, with average SNR contributing additional predictive strength when considered jointly. The findings motivated our subsequent step of dividing the space into distinct modeling domains to better capture variations in quantification behavior.

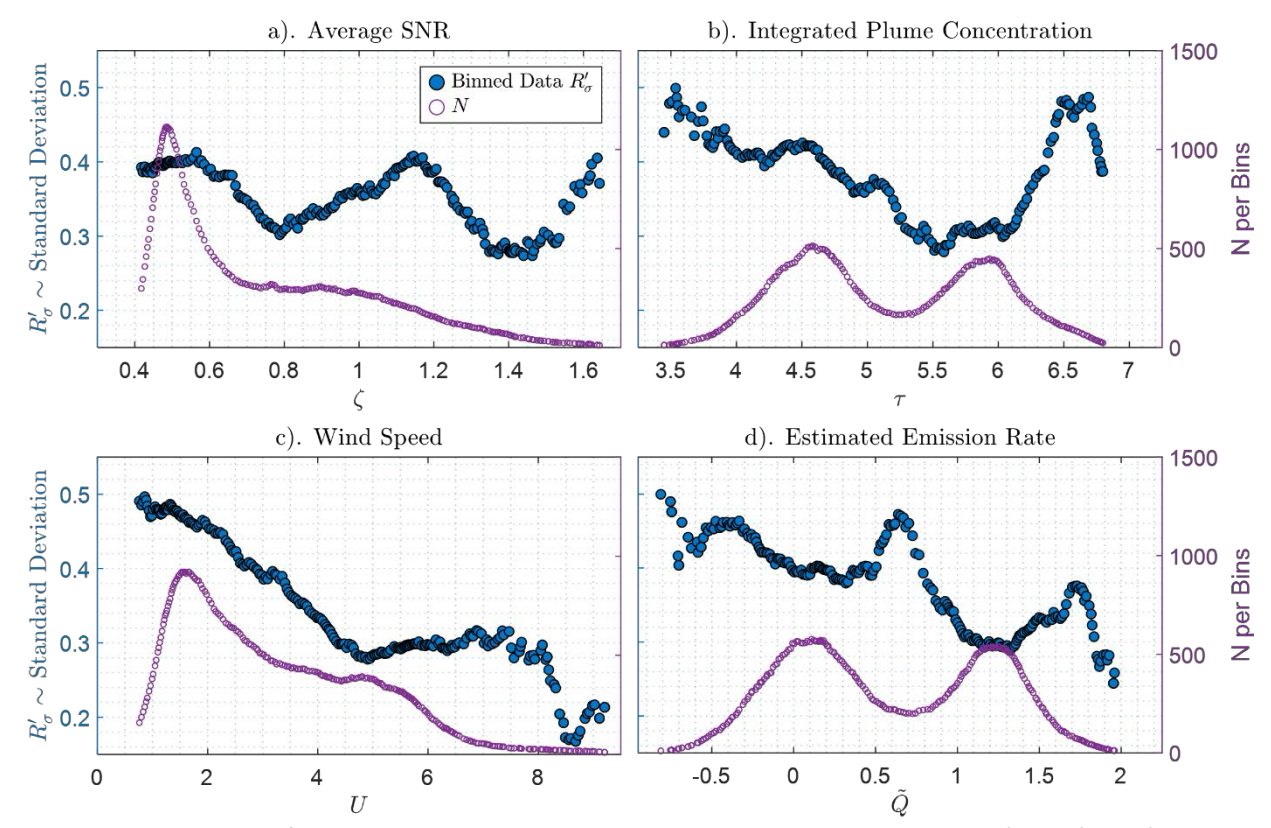


Figure 3. The evolution of uncertainty, measured as the standard deviation, across a): ζ ; b): τ ; c): U; & d): \tilde{Q} . N is the number of data points per bin.

Among the evaluated formulations, predictor B2, which defines a two-dimensional surface in $[\zeta, U]$ -space, achieved the lowest AICc score demonstrating the strongest statistical support. In this model, uncertainty, defined as the standard deviation of logarithmic error (R'), was parameterized as a function of both ζ and U. Along the ζ dimension, uncertainty decreases monotonically with increasing values of average SNR at higher wind speeds, whereas at lower wind speeds, the relationship is partially monotonic, with uncertainty decreasing overall but exhibiting local variability. In the other dimension, increasing U yields monotonically decreasing values of uncertainty.

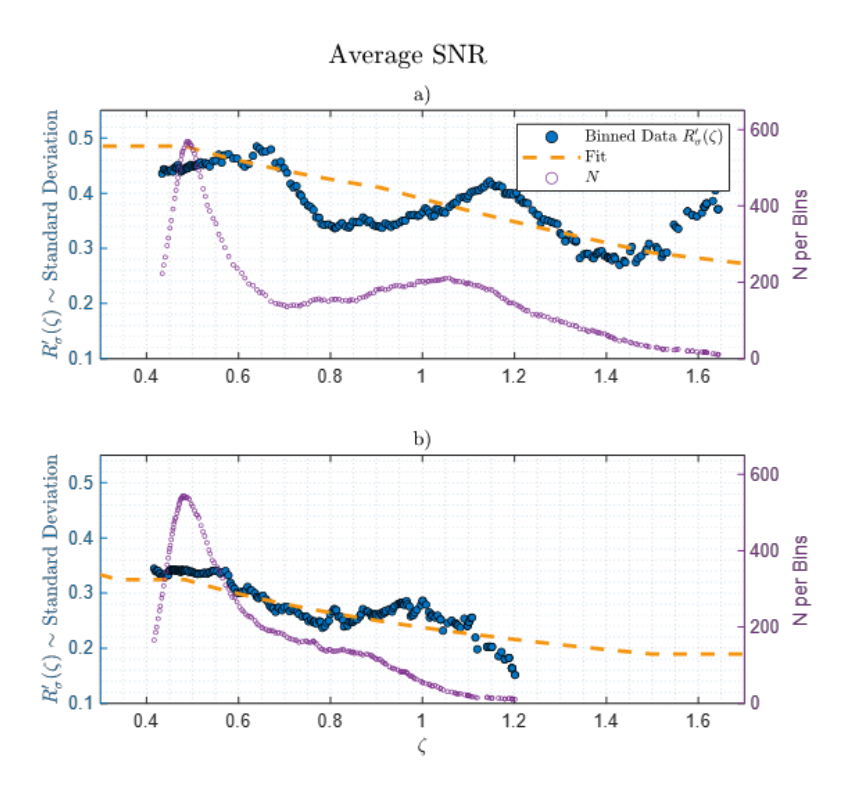


Figure 4. Uncertainty vs ζ , with the complete model fitted uncertainty predictor B2 for a): low wind speeds & b): moderate/high wind speeds.

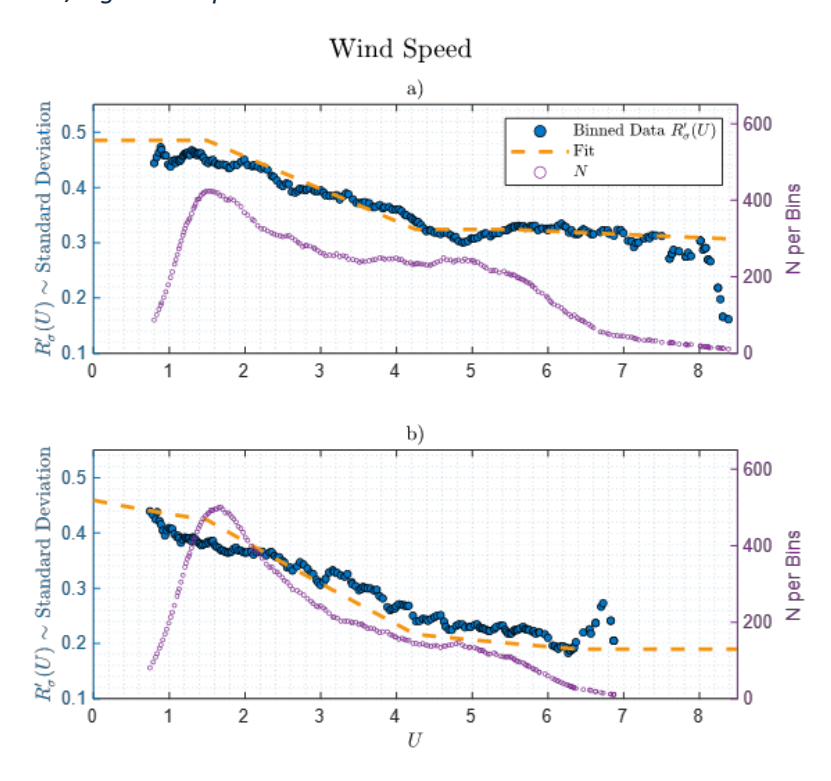


Figure 5. Uncertainty vs U, with the complete model fitted uncertainty predictor B2 for: a): low average SNR & b): moderate/high average SNR.

Overall, ζ primarily governs systematic bias, while uncertainty is jointly influenced by both ζ and U. Retrieval uncertainty decreases systematically with increasing average signal-to-noise ratio (ζ) and higher wind speeds (U). Together, these relationships indicate that higher signal quality and moderate-to-strong winds lead to the most reliable quantification results, as summarized in Table 3.

Table 3. Bias, 90% CI, and corresponding CI lengths across ζ -U regimes. Regimes are defined as low average SNR $(10^{\zeta} \le 3)$, moderate average SNR $(3 < 10^{\zeta} \le 8)$, and high average SNR $(10^{\zeta} > 8)$; low U ($U \le 4$) and high U (U > 4). Bias decreases with increasing ζ , while uncertainty narrows with both higher ζ and U.

Regime	Bias (%)	90 CI (%)	CI Width
Low ζ ; Low U		[-30.1, 195.8]	225.9
Low ζ	43.8	[-21.2, 162.4]	183.6
Low ζ ; High U		[-15.1, 143.4]	158.6
Moderate ζ ; Low U		[-35.9, 150.1]	186
Moderate ζ	26.6	[-28.8, 125.4]	154.2
Moderate ζ ; High U		[-21.5, 104.7]	126.2
High ζ ; Low U		[-43.1, 86.1]	129.2
High ζ	3	[-41.8, 82.6]	124.3
High ζ ; High U		[-28.4, 53.4]	81.7

3.3 Aggregate Model Performance

Complete results for AICc and RLMIL for various model combinations are presented in SI Section S6. Across the full controlled-release dataset, the logistic model paired with predictors A1 B2 (

Table 4) consistently emerged as the highest performing combination. This model balances predictive accuracy with minimum model complexity driven by physical plume characteristics, providing the strongest overall fit. Additionally, the choice model agrees with the prior notion that bias decreases with SNR, and uncertainty declines with increasing SNR and greater wind speeds

(Figure 6).

Table 4 shows useful equations for evaluating the bias correction factor to determine bias corrected emission rates and their associated confidence intervals (CI).

Figure 6 further demonstrates how the fitted logistic model captures the statistical distribution of R' across different ζ regimes (low, moderate, and high). As ζ increases from panels (a) to (c), the R' distributions narrow with bias converging toward zero, reflecting decreasing bias and reduced variance. The agreement between model-predicted and observed bias indicates that the model accurately reproduces the central tendency of the data across all regimes. Low- ζ detections are corrected for their systematic overestimation, while high- ζ detections remain effectively unbiased.

Table 4. Optimized Bias Correction Factor and RER Factor formulations with fitted coefficients, derived from GML 2.0 controlled release dataset. Listed equations are specific to the unclamped region, for

complete details on model form outside of the unclamped region please see Supplementary Information (Section S6.4).

Bias Correction Factor	RER Factor (For Determining Confidence Intervals)	Coefficient Values
BCF(ζ) = $e^{\dot{P}_1(\alpha \mid \zeta)}$, $\dot{P}_1(\alpha \mid \zeta) = \frac{1}{1 + e^{-\alpha_1(\zeta - \alpha_2)}} - 1$	$RER(p \mid [\zeta, U]) = e^{invCDF(\alpha, \beta \mid [\zeta, U], p)},$ $invCDF(\alpha, \beta \mid [\zeta, U], p) = \dot{P}_1(\alpha \mid \zeta) + \dot{P}_2(\alpha, \beta \mid [\zeta, U]) \ln\left(\frac{p}{1-p}\right)$ $= \left(\frac{1}{1 + e^{-\alpha_1(\zeta - \alpha_2)}} - 1\right) + (\beta_1 \ln(\zeta) + \beta_2 U + \beta_3) \ln\left(\frac{p}{1-p}\right)$	$\alpha_1 = 4.4903$ $\alpha_2 = 0.3599$ $\beta_1 = -0.06582$ $\beta_2 = -0.03223$ $\beta_3 = 0.26816$

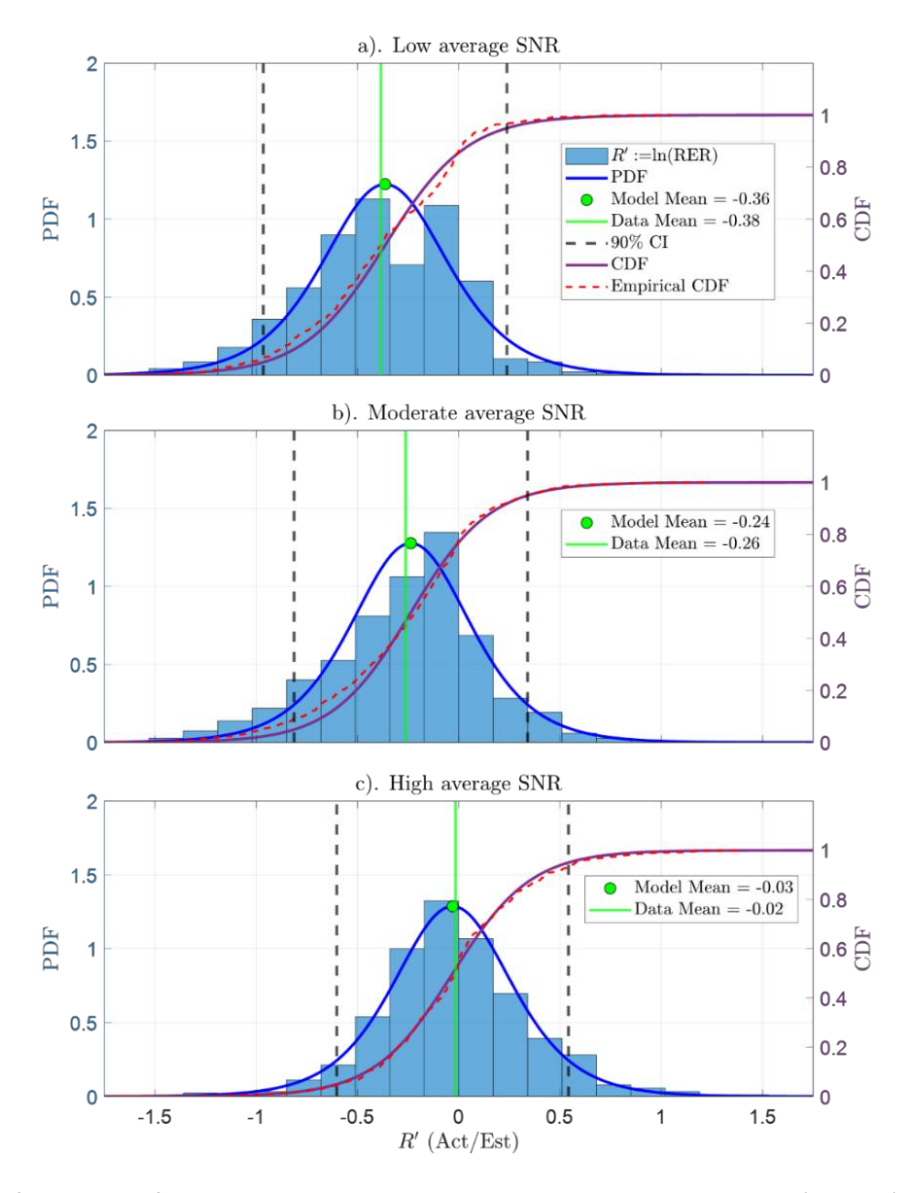


Figure 6. Fits of the quantification error model by average signal to noise ratio: a) low, b) moderate, and c) high.

4 Model Application

4.1 Single Plume Bias Correction and Uncertainty Estimations

The model enables computation of the emission rate bias and uncertainty at a desired confidence interval for individual plumes detected by GML. Bias is computed by inputting average SNR into the pdf distribution, $pdf(\xi^*; \zeta_i)$, to find the distribution mean (R'_{μ}) . R'_{μ} can then be transformed back to linear space to yield the bias correction factor: BCF := RER $_{\mu}$ = exp (R'_{μ}) . Details for constructing the BCF function are found in SI Section 6.4. The bias correction factor is applied to emission rate estimates as a linear scalar to compute the bias corrected emission rate: $\hat{Q} = \text{BCF} \times \tilde{Q}$.

Uncertainty estimates for a single plume emission rate estimate are computed with the average SNR (ζ_i) and wind speed (U_i) using the inverse cumulative distribution function $(invCDF(\xi^*; [\zeta_i, U_i], p))$. Input probabilities (p) define the confidence interval of interest. For example, to get the 90% confidence interval (CI) about the mean of the distribution we evaluate $R_5' = invCDF(\xi^*; [\zeta_i, U_i], 0.05)$ and $R_{95}' = invCDF(\xi^*; [\zeta_i, U_i], 0.95)$. Transforming these values back to a linear space yields RER factors $RER_5 = \exp(R_5')$ and $RER_{95} = \exp(R_{95}')$. These factors are multiplied by the estimated emission rate to produce the 90% CI of the single plume emission rate estimate: $CI_{90} \coloneqq (\hat{Q}_5, \hat{Q}_{95}) = (RER_5 \times \tilde{Q}, RER_{95} \times \tilde{Q})$. To evaluate the standard deviation about the mean, a similar method can be used with a single standard deviation corresponding to the probability density value of $0.3598 \ (\pm 1\sigma = \pm 0.3598)$ for the logistic distribution, more precisely, $(\hat{Q}_{-1\sigma}, \hat{Q}_{+1\sigma}) = \tilde{Q} \times (\exp(R_\mu' - invCDF(\xi^*; [\zeta_i, U_i], 0.3598))$, $\exp(R_\mu' + invCDF(\xi^*; [\zeta_i, U_i], 0.3598))$. An example of the complete evaluation of single plume emission rate quantification error is provided in Table 5.

Table 5. Single plume example summary results. Uncertainties are relative to the bias-corrected estimate.

avgSNR (ζ)	Wind Speed (U; ms ⁻¹)	Actual ER (Q; kgh ⁻¹)	Estimated ER $\left(ilde{Q}; \mathrm{kgh}^{-1} \right)$	BCF	Bias- Corrected ER $\left(\widehat{Q}; \mathrm{kgh}^{-1}\right)$	$\pm 1\sigma$ [%] [kgh $^{-1}$]	90% CI [%] [kgh ⁻¹]
2.27 (0.36)	5.47	1.48	2.02	0.69	1.40	[-27.7, +38.31] [1.02, 1.94]	[-40.93, +69.29] [0.83, 2.38]

4.2 Monte Carlo Application

The QE model can be implemented within a Monte Carlo framework commonly used for inventory development 15,21 . The QE model represents error as a continuous distribution of relative error ratios, which can be sampled during Monte Carlo realizations to propagate error. For each draw of a source, the source's observed average SNR and wind speed are passed as inputs to the QE model to obtain the R' CDF. Optionally, for extrapolation applications, a campaign-level distribution of wind speeds from the deployment can be sampled and used as the wind input for each draw, thereby accounting for variation in deployment conditions across the measurement campaign. A random value is then drawn from the CDF to obtain R' and, subsequently, a bias-correction factor. The measured emission rate is multiplied by this factor to

remove the realization-specific bias, and the updated emission rate is stored for that iteration. Over many iterations, this procedure produces an average emission rate that converges to the bias-corrected mean for that source, while the spread of values across realizations captures the quantification uncertainty interval implied by the QE model.

5 Model Implications

5.1 Error Scaling with Multiple Measurements and Sensors

Obtaining multiple measurements of the same source can reduce quantification error by averaging over random variability. As repeated, independent observations are collected, uncorrelated random errors diminish roughly with the square root of the number of samples $(\frac{1}{\sqrt{N}})$. However, systematic bias arising from correlated over- or underestimation within the measurement system does not diminish through repetition alone and must instead be addressed through bias correction and model calibration.

Known sources of systematic error include sensor-to-sensor calibration variability due to small differences in component performance, sensor construction, or calibration reference conditions. Individual GML 2.0 sensors may exhibit unique calibration biases, meaning that repeated measurements from a single sensor improve precision but remain centered on that sensor's intrinsic bias. When multiple independently calibrated sensors are deployed, these biases tend to cancel through statistical averaging, reducing collective systematic bias approximately as $\frac{1}{\sqrt{M'}}$, where M is the number of sensors. Consequently, total uncertainty depends on both the number of independent measurements (N) and the number of independently calibrated sensors (M): increasing N primarily reduces random uncertainty, while increasing M reduces systematic bias.

For the current GML 2.0 fleet, meaningful reductions in random uncertainty are typically achieved after approximately 5–20 independent measurements of a given source, beyond which additional repetitions yield diminishing returns unless additional independent sensors are introduced. Data on sensor-level variability in bias and uncertainty are presented in SI Section 7. The QE model provides a framework for evaluating both bias and uncertainty at the sensor and technology levels. Because this model characterizes performance across the entire sensor fleet rather than a specific sensor unit, its reduced precision in representing individual deployment bias is compensated by a correspondingly broader uncertainty interval.

5.2 Bias-Correction Effect on Total Emissions

When developing basin or operator total emissions, incorporating the quantification error model mitigates systematic positive bias identified at low SNR. Applied to an aggregate measurement set, the model reduces total estimated emissions. The magnitude of the reduction depends on the measured SNR for each source, and the correction can affect emission rates across the distribution. Estimated emission rate and SNR are distinct and not directly coupled, although some correlation is expected because SNR reflects the measured methane enhancement above background. A small emission often produces only a modest enhancement above background and therefore more commonly yields low SNR, whereas a large emission can

also have low SNR when it is diffuse and the enhancement is spread over a broad area. Other deployment and environmental conditions also influence SNR across the emission rate distribution, such as flight altitude and ground reflectivity.

Figure 7 shows how the magnitude of bias-correction varies across basins with different emission profiles. Panel a) presents cumulative distributions of bias-corrected emission rates for five basins, each with a progressively heavier right-skewed tail toward larger sources. Panel b) shows the corresponding change in basin totals after bias-correction, with an average reduction of about 13.5%. The largest decrease occurs in the Denver–Julesburg Basin at 17.5%, consistent with a profile comprised of more lower rate sources. The Permian Basin has the heaviest upper tail comprised of more large emissions, and its reduction is smallest at 9.8%. This example illustrates that the emissions profile influences the aggregate correction and highlights the need to apply the QE model for measurement-based inventories to remove systematic bias.

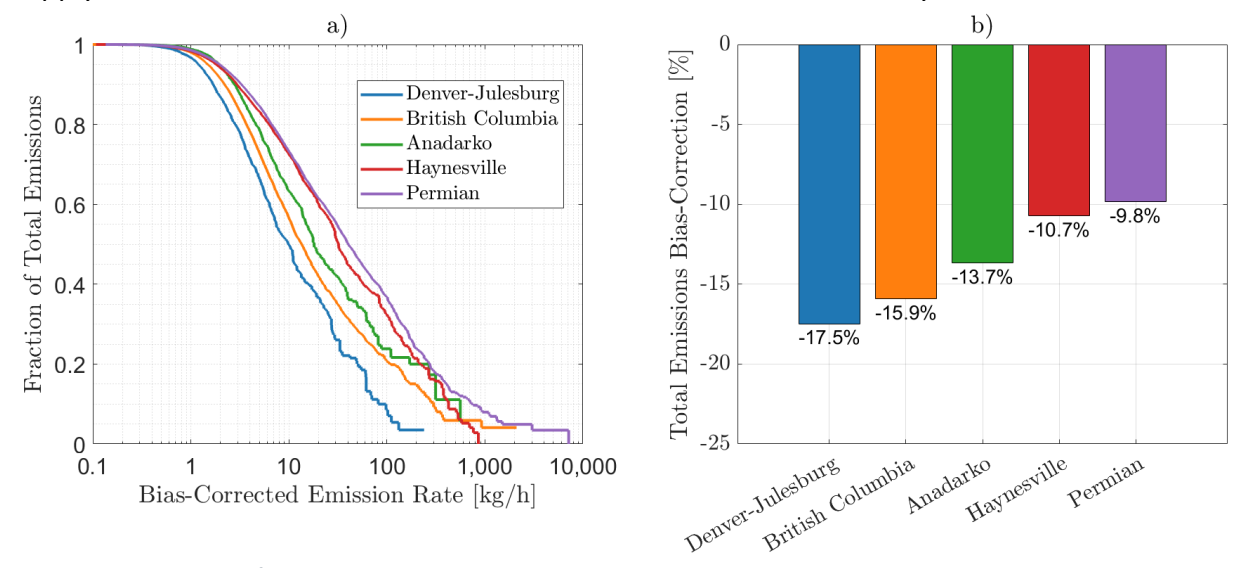


Figure 7. The quantification error model reduces total emissions through bias correction, and the magnitude differs by basin. Panel a) shows basin-level cumulative distributions of bias-corrected emission rates, highlighting differences in emission profiles across basins. Panel b) reports the resulting change in basin totals after bias correction, with larger downward adjustments where lower-rate plumes comprise a greater share of emissions. Note that emission rate and SNR are distinct and not directly coupled, though some correlation exists.

5.3 Model Limitations and Assumptions

The current model was developed exclusively using controlled-release experiments with single, isolated plumes. In the Permian Basin, isolated plumes comprise approximately 66% of detected emissions events in upstream operations and ~46% in midstream operations, representing the low-complexity end of operational conditions where individual plumes can be cleanly resolved and attributed to a single source. Field measurements, however, often contain multiple, overlapping plumes with complex dispersion, partial source coalescence, and correlated uncertainties. To handle such cases, we apply the model by assigning the aggregate plume average SNR to each of its multiple source locations. The bias and uncertainty for each source location are then estimated using the same framework developed for isolated plumes. This

approach ensures consistency and transparency across both simple and complex measurement conditions.

The emission rate quantification error model developed here assumes perfect wind speed information and therefore does not include wind error. Wind error originates from uncertainty in the three-dimensional wind field measurement that is combined with the plume concentration data to estimate an emission rate from the associated source location. Because the transport speed is used as a linear multiplier to convert cross sectional plume concentration into a flow rate, error in the wind speed directly correlates with the total emissions rate error. Decoupling quantification and wind error enables targeted refinement and understanding of each error component, avoiding conflating instrument-driven bias with transport-driven bias and variability. Data collected for this study utilized on site, high-precision and -resolution anemometers to ensure precise understanding of the transport speed of the detected methane plume. For this reason, wind error is considered negligible and absent from data collected in this study enabling a robust examination of the technology's (GML) performance, referred to as quantification error.

This study also assumes detected methane plumes are well thermalized to the local atmospheric temperature. While it is true that many emission sources from oil and gas infrastructure are products of combustions processes, emitted from flare or exhaust stacks. These plumes typically thermalize rapidly once in the atmosphere and present signatures in emission rate analysis that indicate adequate thermalization¹⁷.

6 Discussion

6.1 Critical Takeaways

The QE framework presented here establishes a statistically consistent foundation for estimating emission rate bias and uncertainty across a broad range of measurement conditions. By integrating the predictor inverse-link formulation with measurable predictor parameters, logistic error characterization, and scalable aggregation methods, the model enables transparent uncertainty propagation from individual plume detections to multi-measurement and multisource analyses. The implementation also provides a robust approach for technology-level quantification performance assessment and provides insights into the physical properties of the measurement error. For instance, it may be natural to expect bias to increase at low SNR because systematic errors in estimating the concentration threshold separating the local background concentration and the plume enhancement will lead to systematic errors in the emission rate estimate. Modeling efforts like the work presented here highlight connections between trends in test data and details of the physical measurement. The resulting model provides better measurement characterization and more accurate methane emission rate estimates with robust uncertainty estimates for individual sources, which are key ingredients for building accurate and reliable emissions inventories. We demonstrate the bias correction can reduce systematic errors in inventory estimates by up to 17.5%. This represents a substantial improvement in accuracy and is likely to be even greater for measurement systems that are less sensitive or more affected by environmental parameters.

6.2 Future Work

Future work will focus on extending the model framework to account for limitations of the current QE model. Multi-emitter scenarios are particularly challenging to address, where overlapping source contributions may modify the statistical structure of both bias and uncertainty for individual plume estimates. Additionally, further development is needed to implement existing wind error characterization, as demonstrated in Johnson et. al.²², as a separate source of bias and uncertainty. Paired with the QE model, wind error characterization will provide a complete handling of error associated with estimating methane emission rates using aerial LiDAR technology.

Conflict of Interest Disclosure

Bridger Photonics, Inc. profits from sales of Gas Mapping LiDAR methane emissions monitoring services.

Author Contributions

Cameron D. Dudiak: Writing – review & editing, Writing – original draft, Visualization, Validation, Methodology, Model development, Software, Conceptualization. **Michael J. Thorpe:** Writing – review & editing, Methodology, Model development, Conceptualization. **Devin B. Goodwin:** Writing – review & editing, Writing – original draft, Visualization, Validation, Model development, Software. **Dominic T. Altamura:** Writing – review & editing, Methodology, Model development, Software. **Christopher P. Donahue:** Writing – review & editing, Visualization.

Funding Sources

Bridger Photonics, Inc.

Acknowledgements

Bridger Photonics, Inc. thanks ARPA-E and the Montana Board of Research and Commercialization Technology for support in developing the Gas Mapping LiDAR hardware. We would also like to thank Dr. Jason Brasseur, Dr. Peter Roos, and Aaron Kreitinger for their outstanding work in developing Gas Mapping LiDAR.

References

- (1) Shindell, D.; Ravishankara, A.; Kuylenstierna, J. C.; Michalopoulou, E.; Höglund-Isaksson, L.; Zhang, Y.; Seltzer, K.; Ru, M.; Castelino, R.; Faluvegi, G. *Global Methane Assessment: Benefits and Costs of Mitigating Methane Emissions*; 9280738542; United Nations Environment Programme, 2021.
- (2) Alvarez, R. A.; Zavala-Araiza, D.; Lyon, D. R.; Allen, D. T.; Barkley, Z. R.; Brandt, A. R.; Davis, K. J.; Herndon, S. C.; Jacob, D. J.; Karion, A.; Kort, E. A.; Lamb, B. K.; Lauvaux, T.; Maasakkers, J. D.; Marchese, A. J.; Omara, M.; Pacala, S. W.; Peischl, J.; Robinson, A. L.; Shepson, P. B.; Sweeney, C.; Townsend-Small, A.; Wofsy, S. C.; Hamburg, S. P. Assessment of Methane Emissions from the U.S.

- Oil and Gas Supply Chain. *Science* **2018**, *361* (6398), 186–188. https://doi.org/10.1126/science.aar7204.
- Zavala-Araiza, D.; Lyon, D. R.; Alvarez, R. A.; Davis, K. J.; Harriss, R.; Herndon, S. C.; Karion, A.; Kort, E. A.; Lamb, B. K.; Lan, X.; Marchese, A. J.; Pacala, S. W.; Robinson, A. L.; Shepson, P. B.; Sweeney, C.; Talbot, R.; Townsend-Small, A.; Yacovitch, T. I.; Zimmerle, D. J.; Hamburg, S. P. Reconciling Divergent Estimates of Oil and Gas Methane Emissions. *Proc. Natl. Acad. Sci. U.S.A.* **2015**, *112* (51), 15597–15602. https://doi.org/10.1073/pnas.1522126112.
- (4) Jacob, D. J.; Turner, A. J.; Maasakkers, J. D.; Sheng, J.; Sun, K.; Liu, X.; Chance, K.; Aben, I.; McKeever, J.; Frankenberg, C. Satellite Observations of Atmospheric Methane and Their Value for Quantifying Methane Emissions. *Atmospheric Chemistry and Physics* **2016**, *16* (22), 14371–14396. https://doi.org/10.5194/acp-16-14371-2016.
- (5) Turner, A. J.; Jacob, D. J.; Benmergui, J.; Wofsy, S. C.; Maasakkers, J. D.; Butz, A.; Hasekamp, O.; Biraud, S. C. A Large Increase in U.S. Methane Emissions over the Past Decade Inferred from Satellite Data and Surface Observations. *Geophysical Research Letters* **2016**, *43* (5), 2218–2224. https://doi.org/10.1002/2016GL067987.
- (6) Sherwin, E.; El Abbadi, S.; Burdeau, P.; Zhang, Z.; Chen, Z.; Rutherford, J.; Chen, Y.; Brandt, A. Single-Blind Test of Nine Methane-Sensing Satellite Systems from Three Continents; preprint; Atmospheric Sciences, 2023. https://doi.org/10.31223/X56089.
- (7) Jiang, Y.; Zhang, L.; Zhang, X.; Cao, X. Methane Retrieval Algorithms Based on Satellite: A Review. *Atmosphere* **2024**, *15* (4). https://doi.org/10.3390/atmos15040449.
- (8) Cheptonui, F.; Emerson, E.; Ilonze, C.; Day, R.; Levin, E.; Fleischmann, D.; Brouwer, R.; Zimmerle, D. J. Assessing the Performance of Emerging and Existing Continuous Monitoring Solutions under a Single-Blind Controlled Testing Protocol. *Elementa: Science of the Anthropocene* **2025**, *13* (1), 00020. https://doi.org/10.1525/elementa.2025.00020.
- (9) Cusworth, D. H.; Duren, R. M.; Thorpe, A. K.; Olson-Duvall, W.; Heckler, J.; Chapman, J. W.; Eastwood, M. L.; Helmlinger, M. C.; Green, R. O.; Asner, G. P.; Dennison, P. E.; Miller, C. E. Intermittency of Large Methane Emitters in the Permian Basin. *Environ. Sci. Technol. Lett.* **2021**, *8* (7), 567–573. https://doi.org/10.1021/acs.estlett.1c00173.
- (10) El Abbadi, S. H.; Chen, Z.; Burdeau, P. M.; Rutherford, J. S.; Chen, Y.; Zhang, Z.; Sherwin, E. D.; Brandt, A. R. Technological Maturity of Aircraft-Based Methane Sensing for Greenhouse Gas Mitigation. *Environ. Sci. Technol.* **2024**, *58* (22), 9591–9600. https://doi.org/10.1021/acs.est.4c02439.
- (11) Narayanan, N.; Daun, K.; Talebi-Moghaddam, S. *Quantification Accuracy of Airborne Long-Wave Infrared Hyperspectral Imaging for Detecting Methane Emissions from Upstream Oil and Gas Facilities*; 2025.

- (12) Johnson, M. R.; Tyner, D. R.; Szekeres, A. J. Blinded Evaluation of Airborne Methane Source Detection Using Bridger Photonics LiDAR. *Remote Sensing of Environment* **2021**, *259*, 112418. https://doi.org/10.1016/j.rse.2021.112418.
- (13) Bell, C.; Rutherford, J.; Brandt, A.; Sherwin, E.; Vaughn, T.; Zimmerle, D. Single-Blind Determination of Methane Detection Limits and Quantification Accuracy Using Aircraft-Based LiDAR. *Elementa: Science of the Anthropocene* **2022**, *10* (1), 00080. https://doi.org/10.1525/elementa.2022.00080.
- (14) Thorpe, M. J.; Kreitinger, A.; Altamura, D. T.; Dudiak, C. D.; Conrad, B. M.; Tyner, D. R.; Johnson, M. R.; Brasseur, J. K.; Roos, P. A.; Kunkel, W. M. Deployment-Invariant Probability of Detection Characterization for Aerial LiDAR Methane Detection. *Remote Sensing of Environment* **2024**, *315*, 114435.
- (15) Donahue, C. P.; Oberoi, K.; Dillon, J.; Hengst, V.; Kennedy, B.; Kearney, W.; Lennox, J.; Rehbein, E.; Sykes, R.; Dudiak, C. Aerial LiDAR Based, Source Resolved Methane Emissions Inventory: Permian Basin Case Study for Benchmarking US Emissions. EarthArXiv 2025. https://doi.org/10.31223/X5S45T.
- (16) Conrad, B. M.; Tyner, D. R.; Johnson, M. R. Robust Probabilities of Detection and Quantification Uncertainty for Aerial Methane Detection: Examples for Three Airborne Technologies. *Remote Sensing of Environment* **2023**, *288*, 113499. https://doi.org/10.1016/j.rse.2023.113499.
- (17) Thorpe, M. J.; Kreitinger, A. T. Apparatuses and Methods for Gas Flux Measurements. US12066353B2, August 20, 2024.
- (18) Bland, J. M.; Altman, D. G. Statistics Notes: Transformations, Means, and Confidence Intervals. *BMJ* **1996**, *312* (7038), 1079. https://doi.org/10.1136/bmj.312.7038.1079.
- (19) Lagarias, J. C.; Reeds, J. A.; Wright, M. H.; Wright, P. E. Convergence Properties of the Nelder--Mead Simplex Method in Low Dimensions. *SIAM J. Optim.* **1998**, *9* (1), 112–147. https://doi.org/10.1137/S1052623496303470.
- (20) Portet, S. A Primer on Model Selection Using the Akaike Information Criterion. *Infectious Disease Modelling* **2020**, *5*, 111–128. https://doi.org/10.1016/j.idm.2019.12.010.
- (21) Johnson, M. R.; Conrad, B. M.; Tyner, D. R. Creating Measurement-Based Oil and Gas Sector Methane Inventories Using Source-Resolved Aerial Surveys. *Commun Earth Environ* **2023**, *4* (1), 139. https://doi.org/10.1038/s43247-023-00769-7.

Supporting Information for

Quantification Error Model for Aerial LiDAR Methane Emission Rate Estimates

Cameron D. Dudiak*, Devin B. Goodwin, Dominic T. Altamura, Christopher P. Donahue, and Michael J. Thorpe*

Bridger Photonics, Inc., Bozeman, MT 59715, USA

*Corresponding Authors

Email: Cam.Dudiak@bridgerphotonics.com and Mike.Thorpe@bridgerphotonics.com

Contents

S1. Glossary of Terms	22
S2. Data Distribution	23
S3. Model Parameters	24
S3.1 Estimated Emission Rate	24
S3.2 Average Signal-to-Noise Ratio	25
S3.3 Wind Speed	25
S3.4 Atmospheric Pressure and Ambient Temperature	25
S3.5 Integrated Plume Concentration	26
S4. Transformation of Variables	27
S5. Emission Rate Quantification Error Model and Optimization Scheme	28
S5.1 Weighting Methodology	28
S5.2 Predictor Function Construction and Initial Evaluation	29
S5.3 MLE Model Fitting, Performance Comparison and Model Selection	30
S6. QE Models	31
S6.1 Candidate Predictor Functions	31
S6.2 Candidate Models for All Physical Parameters	32
S6.3 Candidate Models for Selected Physical Parameters	33
S6.4 Detailed Model Definition	35
S7. Sensor-Level Bias and Uncertainty	37
S8. References	38

S1. Glossary of Terms

Table S6 summarizes the acronyms and definitions used throughout both the main manuscript and supporting information. Acronyms are defined at first mention and used consistently thereafter.

Table S6. Acronyms and definitions used throughout both the manuscript and SI.

Acronym	Definition
AIC	Akaike Information Criterion
AICc	Corrected Akaike Information Criterion
AGL	Above Ground Level
ВС	British Columbia
ВР	Bridger Photonics
CI	Confidence Interval
CMS	Continuous Monitoring Systems
CSU	Colorado State University
CU	Carleton University
DJ	Denver-Julesburg
EDF	Environmental Defense Fund
ER	Emission Rate
GML	Gas Mapping LiDAR 2.0
IPC	Integrated Plume Concentration
IR	Infrared
LiDAR	Light Detection and Ranging
LWIR	Long Wave Infrared
METEC	Methane Emissions Technology Evaluation Center
MLE	Maximum Likelihood Estimation
MT	Montana
NLL	Negative Log-Likelihood
NLLF	Negative Log-Likelihood Function
NMSA	Nelder Mead Simplex Algorithm

Probability of Detection PoD **Quantification Error** QE Relative Error Ratio RER Relative Likelihood of Minimizing Information Loss RLMIL Signal-to-Noise Ratio **SNR** Sum of Squared Error SSE **Short Wave Infrared SWIR** Wind Error WE Wind Speed WS

S2. Data Distribution

Figure S8 presents histograms of wind speed conditions and plume properties, including average signal-to-noise ratio (average SNR; $\zeta \coloneqq \log_{10}(\text{average SNR})$), wind speed at the plume location (U; ms^{-1}), integrated plume concentrations (IPC; $\tau \coloneqq \log_{10}(\text{IPC})$; $\text{ppm} \cdot \text{m}^2$), and metered emission rates (Actual ER; $Q \coloneqq \text{Actual ER}$; kgh^{-1}) for each plume in the controlled release data set. Average SNR values varied from 2.2 to 70.8 ($\zeta \in [0.34,1.85]$), with an average of 6.49 ($\zeta_{\mu} = 0.81$), and with approximately 54% of detections falling within the lower end of the average SNR domain ($10^{\zeta} \in [2.2,4]$). Wind speeds conditions during the controlled release tests varied from 0.23 to 9.8 ms⁻¹, with an average of 2.99 ms⁻¹.

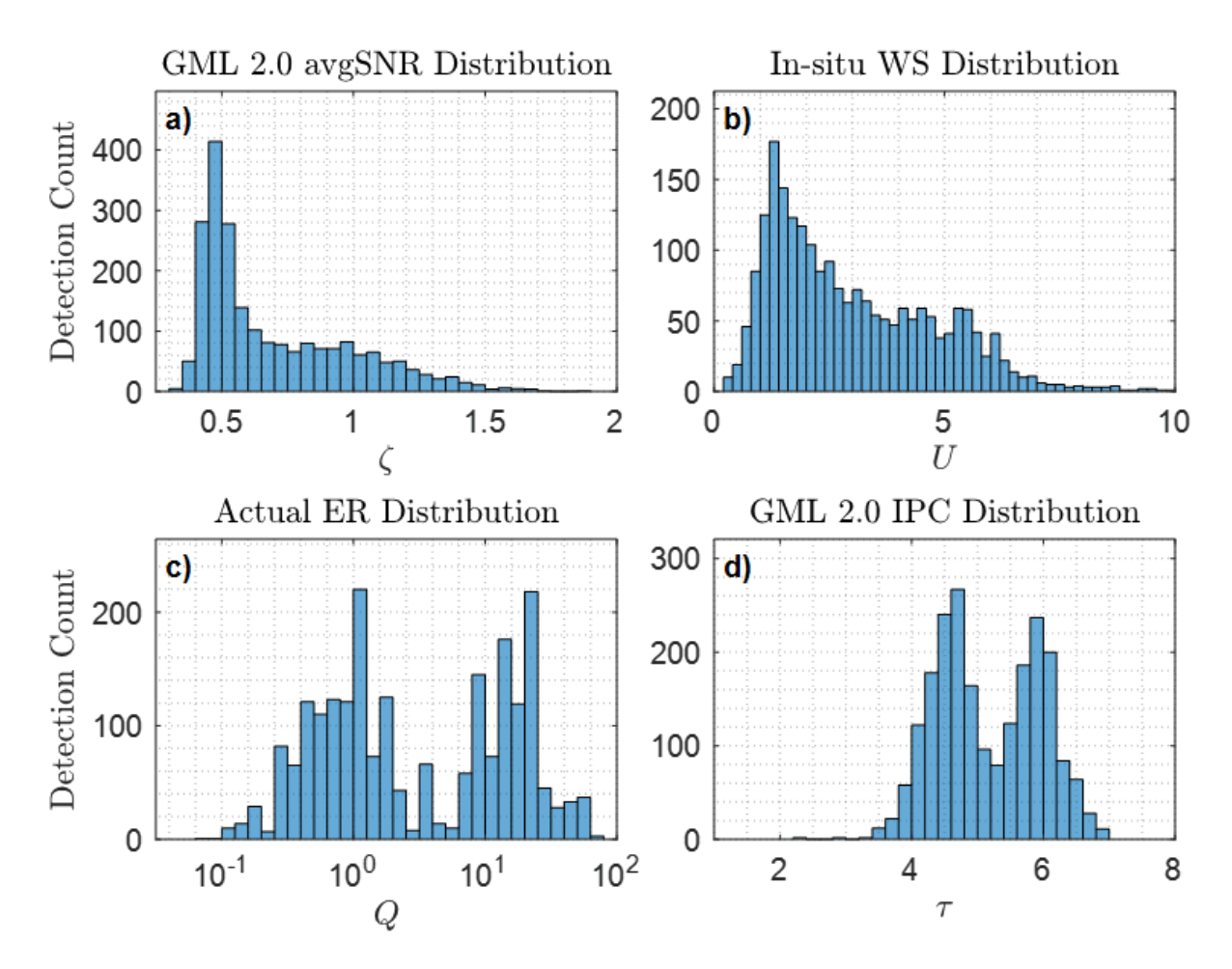


Figure S8. Histograms show the a): GML 2.0 average signal-to-noise ratio (ζ); b): in-situ wind speed (U; ms^{-1}); c): actual emission rate (Q; kgh^{-1}) & d): GML 2.0 integrated plume concentration (τ ; $ppm-m^2$) distributions for the controlled release tests.

S3. Model Parameters

S3.1 Estimated Emission Rate

Emission rate (ER) estimates for detected sources are computed from plume concentration measurements and wind speed data using the method described in Thorpe and Kreitinger¹. The wind speed is estimated at the average height of the detected plume height using the logarithmic wind profile in Eq. (1). The observed wind speed $U(z_1)$ at anemometer height (z_1) and the plume height (z_2) are input into Eq. (1) to produce an estimated wind speed at the plume height $U(z_2)$.

$$U(z_2) = U(z_1) \frac{\ln\left(\frac{z_2 - d}{z_0}\right)}{\ln\left(\frac{z_1 - d}{z_0}\right)},\tag{1}$$

Here, $d=0.066~\rm m$, and $z_0=0.01~\rm m^{2,3}$. The height scaled wind speed is used as a linear multiplier to determine the estimated emission rate.

S3.2 Average Signal-to-Noise Ratio

GML 2.0 measures path-integrated methane concentration measurements at a frequency of 13,333 Hz. At the average fixed-wing flight speed of 160 kph and altitude of 200 m, this results in an average LiDAR point density of 1.51 pts/m². For each LiDAR concentration measurement (C_i), the gas concentration noise (GCN_i) is computed using a calibrated noise model, described in Thorpe et al.³.

The C_i and GCN_i values are projected onto a plane at the average plume height and rasterized to a $1.5 \, \mathrm{m} \times 1.5 \, \mathrm{m}$ resolution grid. The result is a grided gas concentration (GC_j) and grided gas concentration noise (GCN_j) value per pixel j; Details regarding the mathematical formulations of GC_j and GCN_j can be found in Thorpe et al.³. For each pixel, the gridded SNR is defined as the pixel-wise division of rasterized gas concentration by gas concentration noise. A simple average is then taken over the pixels within the detection region, whose SNR exceeds a fixed threshold, to calculate the detection's average SNR, denoted ζ :

$$\zeta = \log_{10} \left(\frac{1}{|N|} \sum_{j \in D} SNR_j \right), \tag{2}$$

where $SNR_j = \frac{GC_j}{GCN_j}$, and N denotes the number of pixels within the detection plume region D exceeding the threshold. Average SNR represents the average strength of methane concentration in the detected plume relative to the noise floor of monitoring technology.

S3.3 Wind Speed

Wind speed measurements for the controlled release flyover tests were taken using the anemometers described in Thorpe, et al.³. The anemometers were placed within 10 m of the controlled release location at a height of 1.5-3.0 m above ground level and away from structures or foliage that could disturb wind flow. The wind speed value used in the QE model is same as the wind speed used for the estimated emission rate, as described in S3.1.

Because the wind speed is measured in close proximity to the release location, error in the estimated emission rate due to errors in the wind speed estimates are assumed to be negligible. Formulating the QE model in this way decouples the contributions wind speed error from other quantification error sources, allowing them to be treated separately.

S3.4 Atmospheric Pressure and Ambient Temperature

Both temperature and pressure affect the absorption properties of methane that are probed by the LiDAR gas concentration measurements⁴. Inaccurate estimation of the temperature and pressure at methane plume location or errors in the computation that converts the LiDAR absorption signal to methane concentration can lead to systematic errors in the emission rate

estimate. Figure S9 shows that both bias and uncertainty remain broadly stable across both parameters, showing no significant dependence on either parameter.

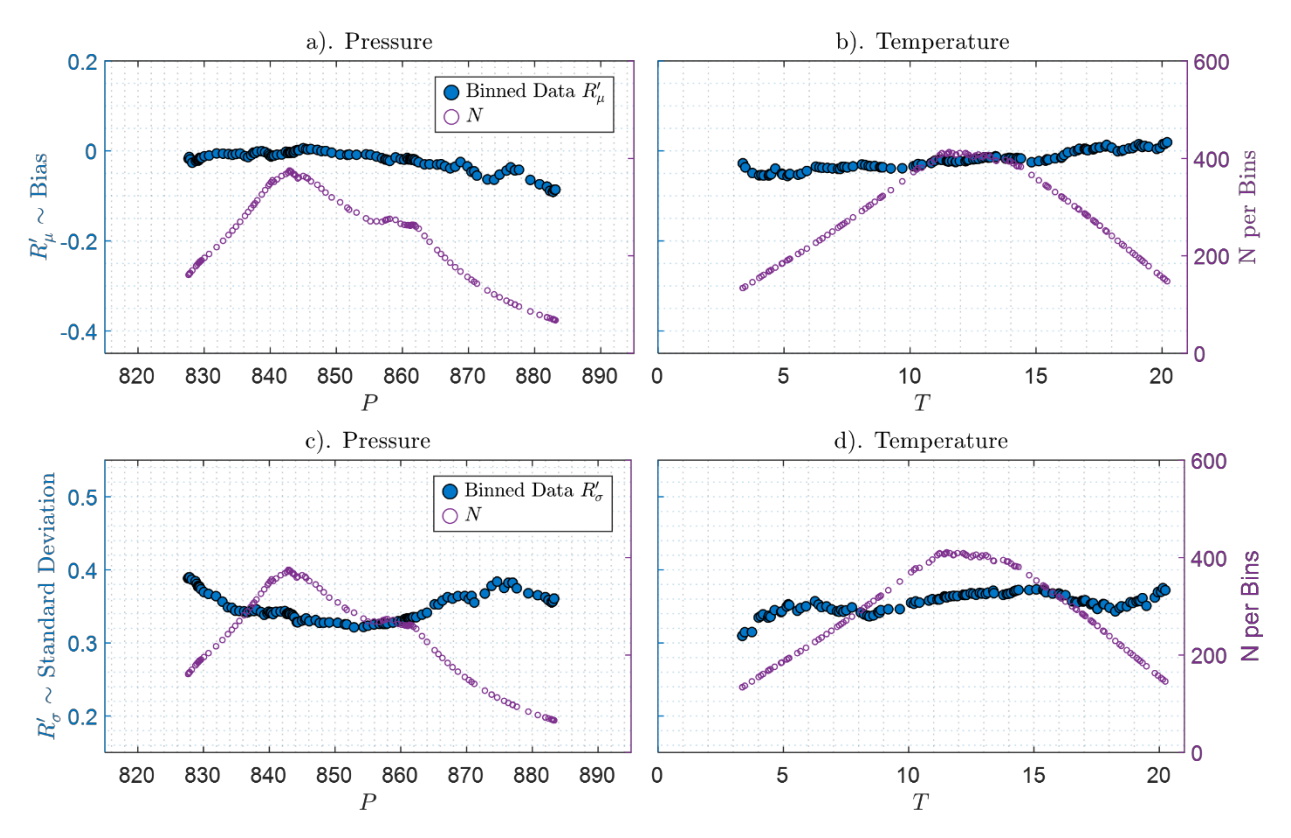


Figure S9. Trends in bias and uncertainty across atmospheric pressure (P [kPa]; panels a and c) and ambient temperature (T [C°]; panels b and d). Only data in the minimal bias and uncertainty regime are considered ($\{x_i \in X \mid \zeta_i \geq 0.95, U_i > 4\}$). N denotes the number of data points per non-disjoint bin.

S3.5 Integrated Plume Concentration

Another metric to quantify methane gas presence is the integrated plume concentration (IPC). IPC represents the total detected gas concentration within a plume and is computed by summing pixel concentration values across both spatial dimensions. A base-10 logarithmic transformation is then applied to create τ :

$$\tau = \log_{10}(IPC) = \log_{10}\left(\sum_{i=1}^{N_I} \sum_{j=1}^{N_J} GC_{i,j}\right),\tag{3}$$

where N_J and N_I denote the total number of pixels along the vertical and horizontal axes of the entire detection region, respectively. Defining τ as the logarithm of IPC allows comparison of detections across multiple orders of magnitude.

S4. Transformation of Variables

Relative error ratio (RER) is defined as the ratio of the actual controlled release emission rate to the emission rate estimated by GML. RER values equal to one indicate a perfect estimation, values less than one indicate overestimation, and values greater than one indicate underestimation. Because RER is bound on the low end by zero, the distribution of RER is inherently asymmetric. Reparametrizing RER using:

$$R' = \ln(\text{RER}),\tag{4}$$

transforms the multiplicative error into additive error on the log scale and produces a symmetric and interpretable distribution of errors, enabling the use of logistic and normal link functions with parameters that directly describe location and scale. However, this change alters the underlying dataset as RER and R' are not the same variable, and models trained on them are not directly comparable through standard information criteria⁵.

Metrics such as the corrected Akaike Information Criterion (AICc) and Relative Likelihood of Minimizing Information Loss (RLMIL) require consistency in the data domain, meaning comparisons between models built on RER and those built on R' cannot be interchanged without careful alignment. To achieve alignment, we leverage the well-known change of variables formula for probability functions which states that given a continuous random variable x with probability density function, f(x), and a strictly monotonic and differentiable transformation y = g(x), the transformed PDF, $f_{y}(y)$, is given by:

$$f_{y}(y) = f_{x}(g^{-1}(y)) \left| \frac{d(g^{-1}(y))}{dx} \right|.$$
 (5)

Suppose that RER ~ Log Logistic(α , β), with PDF $f(\alpha, \beta; RER)$ given by:

$$f_{\text{RER}}(\alpha, \beta; \text{RER}) = \frac{\left(\frac{\beta}{\alpha}\right) \left(\frac{\text{RER}}{\alpha}\right)^{\beta-1}}{\left(1 + \left(\frac{\text{RER}}{\alpha}\right)^{\beta}\right)^{2}}.$$
 (6)

Let $\mu = \ln(\alpha)$ and $s = \frac{1}{\beta}$, then $\alpha = e^{\mu}$, and $\beta = \frac{1}{s}$. Since $\ln(\text{RER})$ is strictly increasing and RER > 0, then it is also differentiable. It follows from Eq. (5) that the PDF for the transformation in Eq. (4) is given by:

$$f_{R'}(\mu, s; R') = f_{RER}(\mu, s; e^{R'}) \left| \frac{d}{dRER} (e^{R'}) \right|$$
$$= \frac{\left(\frac{1}{se^{\mu}}\right) \left(\frac{e^{R'}}{e^{\mu}}\right)^{\frac{1}{s}-1}}{\left(1 + \left(\frac{e^{R'}}{e^{\mu}}\right)^{\frac{1}{s}}\right)^{2}} e^{R'}$$

$$=\frac{e^{\frac{R'-\mu}{s}}}{s\left(1+e^{\frac{R'-\mu}{s}}\right)^2}.$$
 (7)

Eq. (7) implies that $R' \sim \text{Logistic}(\mu, s)$, in other words, if RER $\sim \text{Log Logistic}(\alpha, \beta)$, then $R' = \ln(\text{RER}) \sim \text{Logistic}(\mu, s)$ under the transformation given by Eq. (4).

To compute likelihoods, we can compute directly from the PDF in linear space, for example, for the log-logistic case:

$$\mathcal{L}_{RER} = -\sum_{i=1}^{N} \ln(f_{RER}(\alpha, \beta; RER_i)), \qquad (8)$$

and for the transformed PDF given by Eq. (7):

$$\mathcal{L}_{R'} = -\sum_{i=1}^{N} \ln(f_{R'}(\mu, s; R'_i)) - \ln(\text{RER}_i)$$

$$= -\sum_{i=1}^{N} \ln(f_{R'}(\mu, s; R'_i)) - R'_i$$
(by Eq(5))

The above ensures that likelihoods are computed in comparable spaces. Conversely, if we compute likelihoods directly from the transformed logistic link in log space:

$$\mathcal{L}_{R'} = -\sum_{i=1}^{N} \ln(f_{R'}(\mu, s; R'_i)), \tag{9}$$

then,

$$\mathcal{L}_{RER} = -\sum_{i=1}^{N} \ln(f_{RER}(\alpha, \beta; RER_i)) + RER_i.$$
 (10)

The log-normal/normal case follows a similar logic.

S5. Emission Rate Quantification Error Model and Optimization Scheme

S5.1 Weighting Methodology

To address the issue of non-uniform data density across ζ and U a weighting scheme was constructed to provide uniform data support in the fitting of candidate QE models. For both ζ and U, the data feature vector is normalized using a min-max scaling to the [0,1] range, after which Euclidean distances d_i are computed for every combination of points, $i \neq j$:

$$d_{i} = \sum_{i \neq j}^{N} \sqrt{\left(\zeta_{i} - \zeta_{j}\right)^{2} + \left(U_{i} - U_{j}\right)^{2}} . \tag{11}$$

Similarly for the univariate case:

$$d_{i} = \sum_{i \neq j}^{N} \sqrt{(x_{i} - x_{j})^{2}},$$
(12)

where X denotes one of the evaluated physical parameters $(\zeta, U, \tau, \tilde{Q})$ and x_i its i-th element.

All weights are subsequently normalized to sum to one:

$$w_i = \frac{d_i}{\sum_{k=1}^{N} d_k}. (13)$$

By positively weighing isolated points, this approach ensures that underrepresented regions of the feature space contribute equally to the model optimization process. The weights are then used in the MLE method to optimize the model fit to the data as follows:

$$\xi^* = \underset{\xi}{\operatorname{argmin}} \left(\sum_{i=1}^{N} -\ln(pdf(\xi; x_i)) \times w_i \right). \tag{14}$$

S5.2 Predictor Function Construction and Initial Evaluation

Trends in the mean and standard deviation of $R' = \ln{(\text{RER})}$ distributions are analyzed to determine how they vary as a function of candidate physical parameters. The domain for a given physical parameter space, Y, is partitioned into non-disjoint discrete bins with fixed widths and centers. In this analysis we restrict to one- or two-dimensional partitions. Each bin contains the subset of observations from Y that fall within its bounds, allowing localized estimation of distribution parameters.

Within each bin, both RER and R' are assumed to follow parametric probability distributions (e.g., logistic, normal, log-logistic, or log-normal) – the conditional distribution of these quantities is assumed to be well characterized by such distributions.

For each bin $X_{m,l} = [Y_{m,l}, R'_{m,l}]$, we define the distribution's mean value as:

$$\bar{y}_{m,l} = \frac{1}{N_{m,l}} \sum_{y \in Y_{m,l}} y,$$
 (15)

and use maximum likelihood estimation (MLE) to obtain the best-fit parameters, $\hat{\mu}_{m,l}$ and $\hat{\sigma}_{m,l}$. By examining trends in bias and uncertainty versus physical parameters, we identify functional forms for low order analytical predictor functions:

$$\mu(x) = \dot{P}_1(\alpha; x),\tag{16}$$

$$\sigma(x) = \dot{P}_2(\beta; x),\tag{17}$$

where $x \in X$ denotes a particular value or value pair in the physical parameter space.

We tested the identified predictor functional forms by performing initial ordinary least squares fit to the bin-wise estimates of $(\hat{\mu}_{m,l}, \hat{\sigma}_{m,l})$ to yield the predictor function outputs $(\dot{P}_1(x), \dot{P}_2(x))$. The optimization is carried out with the Nelder-Mead Simplex Algorithm (NMSA)⁶:

$$\alpha_0 = \text{NMSA}\left(\text{SSE}(\dot{P}_1(\bar{y}_{m,l}), \hat{\mu}_{m,l})\right), \tag{18}$$

$$\beta_0 = \text{NMSA}\left(\text{SSE}(\dot{P}_2(\bar{y}_{m,l}), \hat{\sigma}_{m,l})\right). \tag{19}$$

This optimization step yields $\xi_0 = [\alpha_0, \beta_0]$ that serve as initial coefficient estimates for the full QE model MLE fit.

S5.3 MLE Model Fitting, Performance Comparison and Model Selection

The MLE fit is performed by minimizing the weighted negative log-likelihood function, $\mathcal{L}_w(\xi_0; [Y, R']) = -\sum_{i=1}^N \ln \left(f_{R_i'}\left(\xi_0; [Y_i, R_i']\right) \right) \times w_i, \text{ on the un-binned data set using the NMSA to obtain optimized coefficient values, } \xi^*, \text{ for each candidate model:}$

$$\xi^* = [\alpha^*, \beta^*] = \frac{argmin}{\xi} \text{NMSA}(\mathcal{L}_w(\xi_0; [Y, R'])). \tag{20}$$

The minimized negative log-likelihood function evaluation, \mathcal{L}^* is computed from the optimized coefficients in the standard way:

$$\mathcal{L}^* = -\sum_{i=1}^{N} \ln \left(f_{R_i'} \left(\xi^*; [Y_i, R_i'] \right) \right). \tag{21}$$

We repeat the above process for all combinations of links and predictor functions candidates and compute their respective corrected Akaike Information Criterion (AICc) and RLMIL. For each fitted candidate model $m \in M$:

$$AIC_m = 2k_m + 2\mathcal{L}_m^*$$

$$AICc_m = AIC_m + \frac{2k_m(k_m + 1)}{n - k_m - 1},$$
(22)

and

$$RLMIL_m = e^{\frac{AICc^* - AICc_m}{2}},$$
 (23)

where k_m is the number of optimized coefficients, n is the number of datapoints or sample size, and $AICc^* = min(AICc_m)$. The winning model which best fits the data has RLMIL = 1. Note that AICc is constructed to properly account for finite sample sizes, $AICc \rightarrow AIC$, as $n \rightarrow \infty$.

S6. QE Models

S6.1 Candidate Predictor Functions

The list of candidate predictor functions evaluated to represent the location (A#) and shape (B#) of the link function statistical distributions are shown in Table S7. The pair of predictor functions that best represent the controlled release detection data is determined using the optimization process described in the previous section.

Table S7. List of candidate location (\dot{P}_1) and scale (\dot{P}_2) predictor functions tested, with forms defined over all evaluated physical parameters ζ , U, \tilde{Q} , and τ .

Predictors	Functional Form
A1	$\dot{P}_1(\alpha;\zeta) = \frac{1}{1 + e^{\alpha_1(\zeta - \alpha_2)}} - 1$
A2	$\dot{P}_1(\alpha;\zeta) = \frac{\alpha_1}{1 + e^{\alpha_2(\zeta - \alpha_3)}} - \alpha_1$
А3	$\dot{P}_1(\alpha;\zeta) = \frac{1}{1 + e^{\alpha_1(\zeta - \alpha_2)}} - \alpha_3$
A4	$\dot{P}_1(\alpha;\zeta) = \alpha_1 \tan^{-1}(\alpha_2 \zeta + \alpha_3) + \alpha_4$
A5	$\dot{P}_1(\alpha;\zeta) = \alpha_1 \tau + \alpha_2$
A6	$\dot{P}_1(\alpha;\zeta) = \alpha_1 \tilde{Q} + \alpha_2$
A7	$\dot{P}_1(\alpha;\zeta) = \alpha_1 U + \alpha_2$
B1	$\dot{P}_2(\beta;\zeta,U) = \beta_1 \zeta + \beta_2 U + \beta_3$
B2	$\dot{P}_2(\beta;\zeta,U) = \beta_1 \ln(\zeta) + \beta_2 U + \beta_3$
В3	$\dot{P}_2(\beta;\tau) = \beta_1 + \beta_2(\tau - \beta_3)^2$
B4	$\dot{P}_2(\beta;\tau) = \beta_1 \tau + \beta_2$
B5	$\dot{P}_2(\beta;\zeta) = \beta_1 \zeta + \beta_2$
В6	$\dot{P}_2(\beta; \tilde{Q}) = \beta_1 \tilde{Q} + \beta_2$
B7	$\dot{P}_2(\beta; U) = \beta_1 U + \beta_2$

B8
$$\dot{P}_2(\beta; \tilde{Q}) = \beta_1 + \beta_2 (\tilde{Q} - \beta_3)^2$$
B9
$$\dot{P}_2(\beta; U, \tilde{Q}) = \beta_1 U + \beta_2 \tilde{Q} + \beta_3$$
B10
$$\dot{P}_2(\beta; \zeta) = \beta_1 \ln(\zeta) + \beta_2$$

S6.2 Candidate Models for All Physical Parameters

Table S8 illustrates that models incorporating the two-dimensional feature vector $[\zeta, U]$ for Predictor 2, \dot{P}_2 , perform substantially better than those using any single physical parameter, as reflected in both AICc and RLMIL values. This strongly supports the selection of $[\zeta, U]$ as the best-suited input vector for modeling QE.

Table S8. Optimized top performing candidate models for all evaluated physical parameters. The best-performing model, based on the two-dimensional input vector $[\zeta, U]$ with predictors A1 and B2 under a logistic link, is highlighted in green. The second-best model, also using $[\zeta, U]$, but with predictors A1 and B1 under the logistic link, is highlighted in yellow. All remaining models provide negligible support relative to these two candidates.

Link Type	P ₁ Input	P ₂ Input	P ₁ Function	P ₂ Function	#Coeff	NLL	AICc	RLMIL
logistic	ζ	$[\zeta, U]$	A1	B2	5	354.32	718.67	1
logistic	ζ	$[\zeta, U]$	A1	B1	5	354.56	719.15	0.79
logistic	ζ	$\left[ilde{Q},U ight]$	A1	В9	5	366.17	742.37	0
logistic	ζ	U	A1	В7	4	371.33	750.69	0
logistic	ζ	$ ilde{Q}$	A1	B8	5	378.46	766.95	0
logistic	τ	τ	A5	В3	5	386.23	782.49	0
logistic	τ	τ	A5	B4	4	391.38	790.79	0
log logistic	ζ	ζ	A4	B5	6	396.52	805.08	0
logistic	ζ	ζ	A4	B10	6	396.99	806.02	0
logistic	$ ilde{Q}$	$ ilde{Q}$	A6	В6	4	466.40	940.82	0
log logistic	Q	Q	A6	B6	4	466.94	941.91	0
logistic	U	U	A7	В7	4	508.90	1025.83	0

normal U U A7 B7 4 510.03 1028.08 0

S6.3 Candidate Models for Selected Physical Parameters

The A1/B2 predictor function combination, paired with a logistic inverse link function, provides the best representation of bias and uncertainty in the GML 2.0 controlled release data, achieving the highest relative likelihood of minimizing information loss. The A1/B1 combination with a logistic link is the second-best supporting model (RLMIL $\approx 79\%$). Models incorporating predictor functions A2-A4 are less competitive, as marginal reductions in negative log-likelihood fail to offset the penalty associated with additional model parameters (Table S9). Among candidate inverse link functions, the logistic form consistently outperforms the normal, log-logistic, and log-normal alternatives, which offer substantially lower likelihood support.

Table S9. Relative likelihood of minimizing information loss (RLMIL) for candidate QE models fit to GML 2.0 controlled release data. The optimal predictor-link function combination (A1/B2 with logistic link) is highlighted in green; the second-best model (A1/B1 with logistic link) is highlighted in yellow, and the best performing predictor functions are highlighted in blue.

P1 Function	P2 Function	Inverse Link Function	RLMIL
A1	B1	logistic	0.79
A1	B1	log logistic	0.08
A1	B1	normal	0
A1	B1	log normal	0.01
A1	B2	logistic	1
A1	B2	log logistic	0.09
A1	B2	normal	0.01
A1	B2	log normal	0.01

A2	B1	logistic	0.39
A2	B1	normal	0
A2	B1	log normal	0
A2	B2	logistic	0.49
A2	B2	normal	0
A2	B2	log normal	0
A3	B1	logistic	0.39
А3	B1	log logistic	0.03
А3	B1	normal	0
A3	B1	log normal	0.01
A3	B2	logistic	0.49
А3	B2	log logistic	0.03
А3	B2	normal	0
А3	B2	log normal	0
A4	B1	logistic	0.19
A4	B1	log logistic	0.01
A4	B1	normal	0
A4	B1	log normal	0
A4	B2	logistic	0.24
A4	B2	log logistic	0.01
A4	B2	normal	0
A4	B2	log normal	0

S6.4 Detailed Model Definition

The detailed functional form of the QE model is given by:

$$PDF := f(\dot{P}_{1}(\alpha), \dot{P}_{2}(\beta) \mid [\mathbf{Y}, R']) = \frac{e^{\frac{-(R' - \dot{P}_{1}(\alpha \mid \zeta))}{\dot{P}_{2}(\beta \mid [\zeta, \mathbf{U}])}}}{\dot{P}_{2}(\beta \mid [\zeta, \mathbf{U}]) \left(1 + e^{\frac{-(R' - \dot{P}_{1}(\alpha \mid \zeta))}{\dot{P}_{2}(\beta \mid [\zeta, \mathbf{U}])}}\right)^{2}},$$
(24)

$$CDF := F(\dot{P}_1(\alpha), \dot{P}_2(\beta) \mid [\mathbf{Y}, R']) = \frac{1}{1 + e^{\frac{-(R' - \dot{P}_1(\alpha \mid \zeta))}{\dot{P}_2(\beta \mid [\zeta, U])}}},$$

$$(25)$$

$$invCDF := F^{-1}(\dot{P}_1(\alpha), \dot{P}_2(\beta) \mid p]) = \dot{P}_1(\alpha \mid \zeta) + \dot{P}_2(\beta \mid [\zeta, U]) \ln\left(\frac{p}{1-p}\right) , \qquad (26)$$

$$BCF(\zeta) = e^{\dot{P}_1(\alpha \mid \zeta)} \quad , \tag{27}$$

$$RER_{p}([\boldsymbol{\zeta}, \boldsymbol{U}]) = e^{invCDF(\alpha, \beta \mid [\boldsymbol{\zeta}, \boldsymbol{U}], p)} . \tag{28}$$

Because the controlled release data set has limited coverage of the parameter space, both in terms of the release sizes and wind speed, we have clamped the location and scale parameter values outside of the region with adequate data support. This prevents extrapolation beyond the observed domain and improves interpretability of the resulting model coefficients.

For the location parameter, the one-dimensional predictor functional form is defined by the following three cases:

$$\dot{P}_{1}(\alpha; \zeta) = \begin{cases} \frac{1}{1 + e^{-\alpha_{1}(0.485 - \alpha_{2})}} - 1, & if \zeta < 0.485\\ \frac{1}{1 + e^{-\alpha_{1}(\zeta - \alpha_{2})}} - 1, & if \zeta \in [0.485, 1.5]\\ \frac{1}{1 + e^{-\alpha_{1}(1.5 - \alpha_{2})}} - 1, & if \zeta > 1.5 \end{cases}$$
(29)

Where $\alpha = [\alpha_1, \alpha_2]$ is the vector of optimized coefficients for P1. The scale parameter is modeled by the two-dimensional predictor function:

$$\dot{P}_2(\beta; [\zeta, U]) = \beta_1 \ln(\zeta) + \beta_2 U + \beta_3. \tag{30}$$

Where $\beta = [\beta_1, \beta_2, \beta_3]$ is the vector of optimized coefficients for P2. Eq. (30) defines a total of 9 regions where clamping occurs. These regions are shown in Figure S10, and corresponding functional evaluations are listed in Table S10.

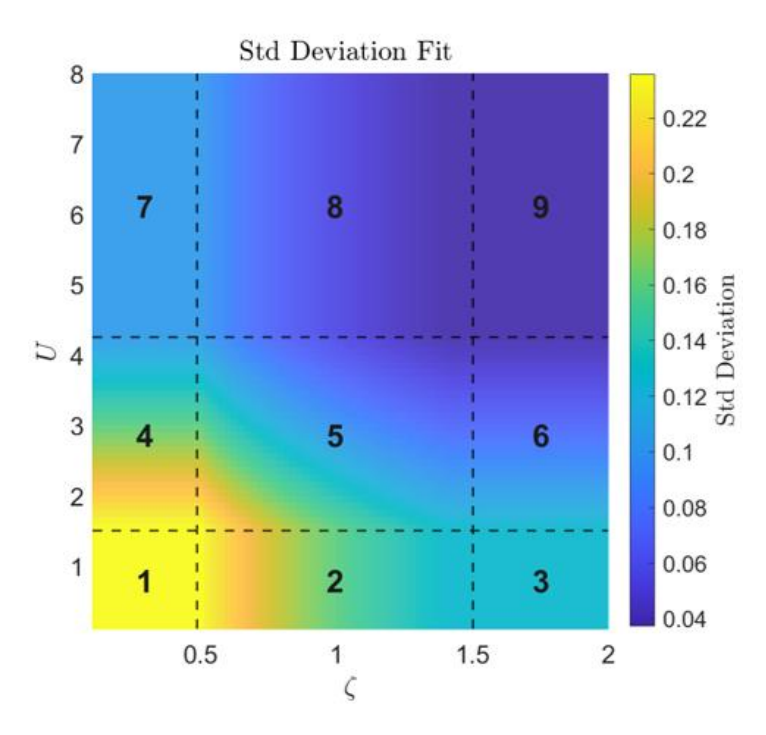


Figure S10. Top-Down view of the fitted surface of the standard deviation predictor as a function of both ζ and U. The color scale indicates the estimated standard deviation, with warmer colors corresponding to higher variability. The dashed black lines divide the parameter space into the nine clamped regions (labeled 1-9).

Table S10. Functional evaluations of the P2 predictor across clamped regions of the parameter space defined by ζ and U. Each region corresponds to the partitioning shown in Figure S4, with domain bounds specified for both ζ and U. Within each region, the predictor reduces to the functional form shown in the rightmost column.

Region	Domain	Functional Evaluation
1	ζ < 0.485 & <i>U</i> < 1.5	$\beta_1 \ln(0.485) + \beta_2(1.5) + \beta_3$
2	$0.485 \le \zeta \le 1.5 \& U < 1.5$	$\beta_1 \ln(\boldsymbol{\zeta}) + \beta_2(1.5) + \beta_3$
3	$1.5 < \zeta \& U < 1.5$	$\beta_1 \ln(1.5) + \beta_2(1.5) + \beta_3$
4	$\zeta < 0.485 \& 1.5 \le U \le 4.25$	$\beta_1 \ln(0.485) + \beta_2 \mathbf{U} + \beta_3$
5	$0.485 \le \zeta \le 1.5 \& 1.5 \le U \le 4.25$	$\beta_1 \ln(\zeta) + \beta_2 U + \beta_3$
6	$1.5 < \zeta \& 1.5 \le U \le 4.25$	$\beta_1 \ln(1.5) + \beta_2 \mathbf{U} + \beta_3$
7	$\zeta < 0.485 \& 4.25 < U$	$\beta_1 \ln(0.485) + \beta_2(4.25) + \beta_3$

8 $0.485 \le \zeta \le 1.5 \& 4.25 < U$ $\beta_1 \ln(\zeta) + \beta_2 (4.25) + \beta_3$ 9 $1.5 < \zeta \& 4.25 < U$ $\beta_1 \ln(1.5) + \beta_2 (4.25) + \beta_3$

S7. Sensor-Level Bias and Uncertainty

Figure S11 shows the average value of $R_{\mu}{}'$ as a function of ζ for individual GML 2.0 sensors with enough controlled release data to support sensor-level characterization. All sensors exhibit a similar shape in their $R_{\mu}{}'$ versus ζ curves as the aggregate data set with a relatively small spread in bias of $\pm 10\%$ compared to the aggregate curve. The sensor-level characterization highlights how individual sensor calibration can contribute upwards of $\pm 10\%$ and how deployment of multiple sensors across larger measurement campaigns can mitigate individual sensor bias and lead to more accurate total emissions estimates.

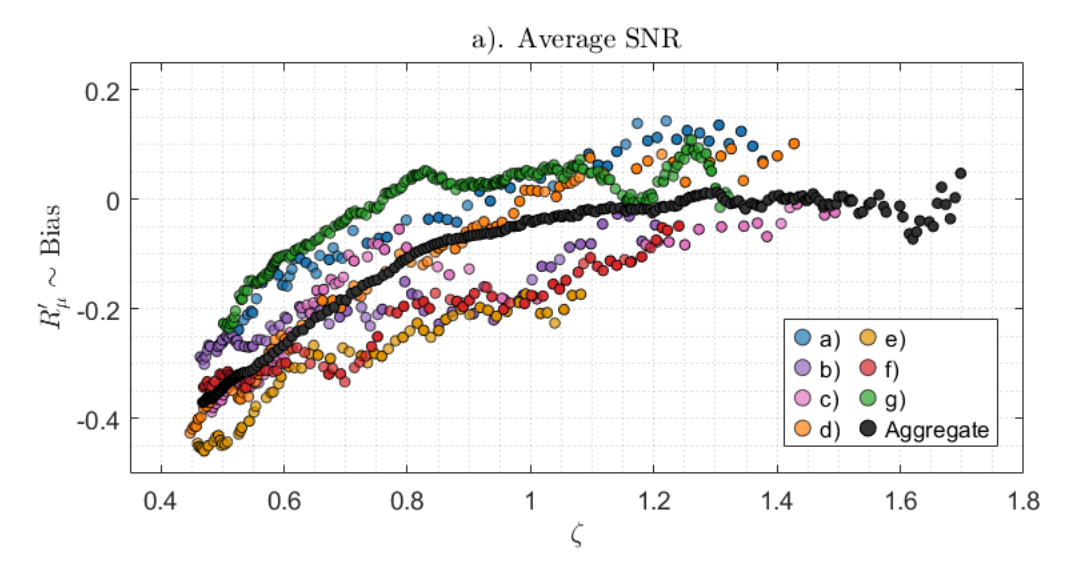


Figure S11. Sensor-level bias evolution as a function of ζ . Each color corresponds to a distinct sensor, with the aggregate response shown in black. At higher ζ , sensor bias remains tightly clustered, with $\sim \pm 10\%$ bands indicating stable and consistent behavior.

Figure S12 shows the average value of $R_{\sigma}{}'$ as a function of ζ and U for individual GML 2.0 sensors. Trends in $R_{\sigma}{}'$ appear less consistent in these figures due to the added complexity of dependence on two parameters. Nonetheless, both individual and aggregate uncertainty, show decreasing uncertainty with increasing ζ and U, reinforcing that stronger SNR and higher wind speed improve precision.

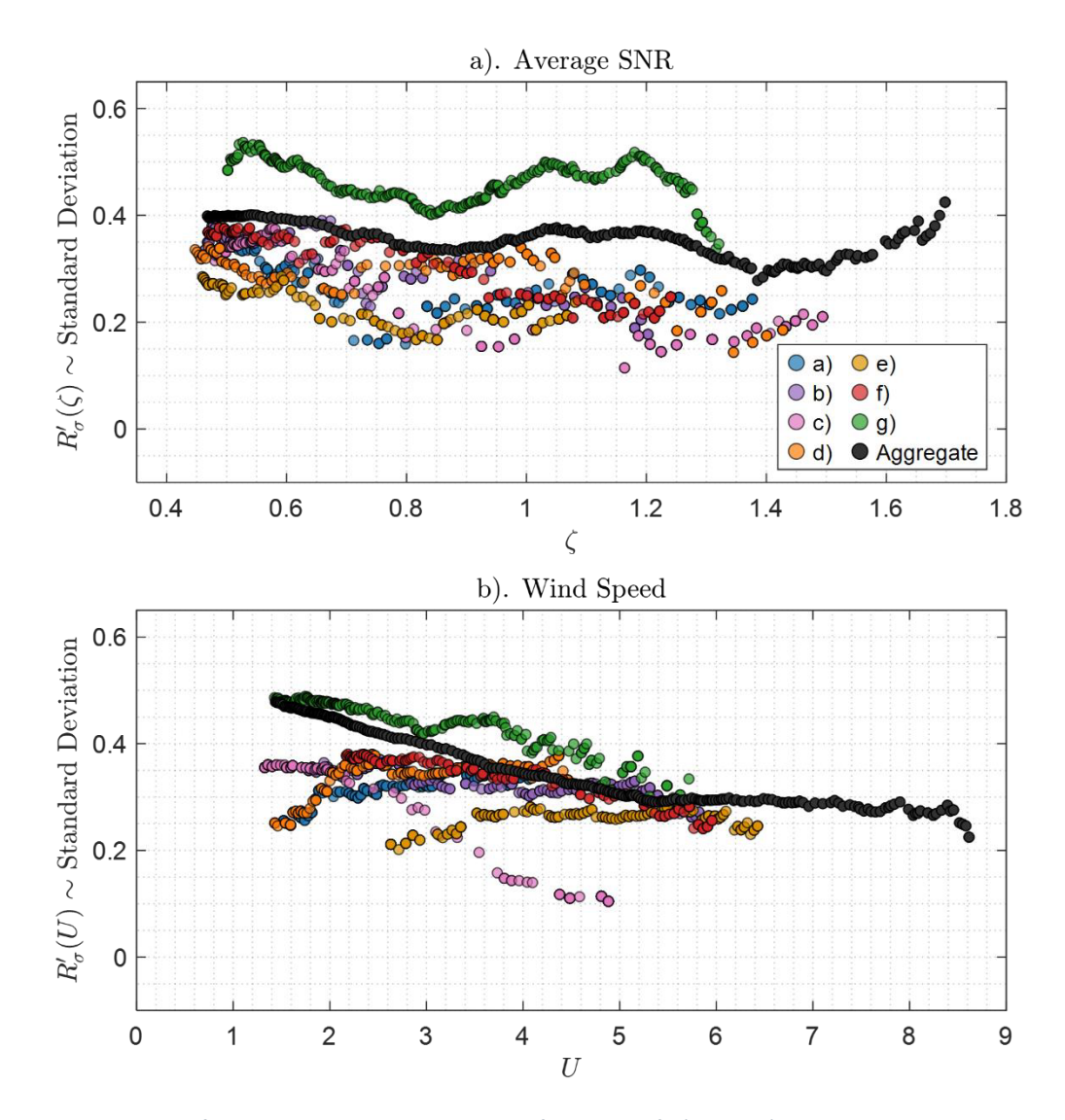


Figure S12. Evolution of the standard deviation as a function of a): ζ & b): U, resolved at the sensor-level. Each colored curve corresponds to a distinct sensor, with the aggregate behavior across all sensors shown in black. Panel a) highlights how variability changes with ζ , while panel b) shows the corresponding trends with respect to U. Together, these plots illustrate both sensor-specific differences in uncertainty and the overall aggregate trend.

S8. References

(1) Thorpe, M. J.; Kreitinger, A. T. Apparatuses and Methods for Gas Flux Measurements. US12066353B2, August 20, 2024.

- (2) Conrad, B. M.; Tyner, D. R.; Johnson, M. R. Robust Probabilities of Detection and Quantification Uncertainty for Aerial Methane Detection: Examples for Three Airborne Technologies. *Remote Sens. Environ.* **2023**, *288*, 113499. https://doi.org/10.1016/j.rse.2023.113499.
- (3) Thorpe, M.; Krietinger, A.; Altamura, D.; Dudiak, C.; Conrad, B.; Tyner, D.; Johnson, M.; Brasseur, J.; Roos, P.; Kunkel, W.; Carre-Burritt, A.; Abate, J.; Price, T.; Yaralian, D.; Kennedy, B.; Newton, E.; Rodriguez, E.; Ibrahim Elfar, O.; Zimmerle, D. Deployment-Invariant Probability of Detection Characterization for Aerial LiDAR Methane Detection. Environmental Monitoring January 26, 2024. https://doi.org/10.31223/X5R96M.
- (4) Brown, L. R.; Sung, K.; Benner, D. C.; Devi, V. M.; Boudon, V.; Gabard, T.; Wenger, C.; Campargue, A.; Leshchishina, O.; Kassi, S.; Mondelain, D.; Wang, L.; Daumont, L.; Régalia, L.; Rey, M.; Thomas, X.; Tyuterev, Vl. G.; Lyulin, O. M.; Nikitin, A. V.; Niederer, H. M.; Albert, S.; Bauerecker, S.; Quack, M.; O'Brien, J. J.; Gordon, I. E.; Rothman, L. S.; Sasada, H.; Coustenis, A.; Smith, M. A. H.; Carrington, T.; Wang, X.-G.; Mantz, A. W.; Spickler, P. T. Methane Line Parameters in the HITRAN2012 Database. *HITRAN2012 Spec. Issue* **2013**, *130*, 201–219. https://doi.org/10.1016/j.jqsrt.2013.06.020.
- (5) Portet, S. A Primer on Model Selection Using the Akaike Information Criterion. *Infect. Dis. Model.* **2020**, *5*, 111–128. https://doi.org/10.1016/j.idm.2019.12.010.
- (6) Lagarias, J. C.; Reeds, J. A.; Wright, M. H.; Wright, P. E. Convergence Properties of the Nelder-Mead Simplex Method in Low Dimensions. *SIAM J. Optim.* **1998**, *9* (1), 112–147. https://doi.org/10.1137/S1052623496303470.